Effects of magma ocean crystallization and overturn on the development of ^{142}Nd and ^{182}W isotopic heterogeneities in the primordial mantle

Stephanie M. Brown[a,*], Linda T. Elkins-Tanton[b], Richard J. Walker[c]

[a]*Department of Earth, Atmospheric, and Planetary Sciences, Massachusetts Institute of Technology, 77 Massachusetts Avenue, Cambridge, MA 02139 United States*
[b]*School of Earth and Space Exploration, Arizona State University, Tempe, AZ 85287, United States*
[c]*Department of Geology, University of Maryland, College Park, MD 20742 United States*

Abstract

One possible mechanism to explain the observed variability of the short-lived ^{146}Sm→^{142}Nd and ^{182}Hf→^{182}W systems recorded in some early Earth rocks is crystal-liquid fractionation and overturn in an early magma ocean. This process could also potentially explain the deviation between the ^{142}Nd isotopic composition of the accessible Earth and the chondritic average. To examine these effects, the magma ocean solidification code of Elkins-Tanton (2008) and a modified Monte Carlo algorithm, designed to randomly choose physically reasonable trace element partition coefficients in crystallizing mantle phases, are used to model the isotopic evolution of early Earth reservoirs. This model, also constrained by the ^{143}Nd composition of the accessible Earth, explores the effects of changing the amount of interstitial liquid trapped in cumulates, the half-life of ^{146}Sm, the magnitude of late accre-

*Principal corresponding author
Email addresses: `brownsm@mit.edu` (Stephanie M. Brown), `ltelkins@asu.edu` (Linda T. Elkins-Tanton), `rjwalker@umd.edu` (Richard J. Walker)

tion, and the simplified model of post-overturn reservoir mixing. Regardless of the parameters used, our results indicate the generation of early mantle reservoirs with isotopic characteristics consistent with observed anomalies is a likely outcome of magma ocean crystallization and overturn of shallow, enriched, and dense (i.e., gravitationally unstable) cumulates. The high-iron composition and density of a hypothesized, early-formed enriched mantle reservoir is compatible with seismic observations indicating large, low-shear velocity provinces (LLSVPs) (e.g., Trampert et al., 2004) present in the mantle today. Later melts of an enriched reservoir are likely to have remained isolated deep within the mantle (e.g., Thomas et al., 2012), consistent with the possibility that the presently observed LLSVPs could be partially or fully composed of remnants of an early enriched reservoir.

---

1. Introduction and Motivation

1.1. The record of ^{142}Nd and ^{182}W variability

High precision isotopic measurements of extinct radionuclides have shed light on the formation and evolution of the early Earth (Caro et al., 2003; Boyet and Carlson, 2005; Willbold et al., 2011). For example, $^{146}\mathrm{Sm} \rightarrow {}^{142}\mathrm{Nd}$ (half-life=103 Myr or 68 Myr) and $^{182}\mathrm{Hf} \rightarrow {}^{182}\mathrm{W}$ (half-life=8.9 Myr) isotopic systematics are ideal for studying early magmatic processes because the parent isotopes became essentially extinct within 500 Myr and 60 Myr, respectively, of Solar System formation. The two systems are also complementary in that they behave differently from the standpoint of geochemical fractionation of parent and daughter elements: Hf, Sm, and Nd are strongly lithophile trace elements, while W is moderately siderophile. Hence, the study of the combined systems can potentially be used to distinguish between various, large-scale, early Earth processes.

Rocks from the lithologically diverse ∼3.8 Ga Isua Greenstone Belt (Caro et al., 2003; Willbold et al., 2011) and the ∼3.8 Ga or ∼4.4 Ga Nuvvuagittuq Greenstone Belt (O'Neil et al., 2008, 2012; Touboul et al., 2014) have resolvable excesses of 10-20 ppm in both ^{182}W and ^{142}Nd; the Nuvvuagittuq suite also preserves ^{142}Nd depletions. Isotopic anomalies for these systems are reported as μ values, which are the deviations from the terrestrial standard in parts per million (ppm). The ∼2.8 Ga komatiites from the Kostomuksha Greenstone Belt also have well resolvable excess μ^{182}W values of ∼14 ppm (Touboul et al., 2012) but a modern μ^{142}Nd value of 0 (Boyet and Carlson, 2006). By contrast, the ∼3.5 Ga Komati komatiites from the Barberton Greenstone Belt are characterized by a modern μ^{142}Nd value of 0 and also a

μ^{182}W that is unresolved from modern ^{182}W (Touboul et al., 2012; Puchtel et al., 2013), which indicates that these isotopic anomalies were not uniformly distributed during early Earth history. Collectively, studies of ^{142}Nd in other early Earth rocks have shown a general, non-linear age trend (Figure 1) of both positive and negative anomalies decreasing towards the present, which largely disappear by $\sim$2.7 Ga (e.g., Rizo et al., 2013). So far only the Isua Greenstone Belt samples appear to record variations in both ^{142}Nd and ^{182}W (Caro et al., 2003; Willbold et al., 2011), but open-system behavior (i.e., W mobility), mixing, or fractionation after ^{182}Hf was no longer extant but before ^{146}Sm became extinct, could have led to a decoupling of the two isotopic systems of the early Earth rocks or their mantle sources (Touboul et al., 2014).

Boyet and Carlson (2005) reported that modern terrestrial rocks have $\sim$20 ppm higher μ^{142}Nd values than the chondritic average. There are at least three possible explanations for this difference: (1) the Earth formed from primitive materials enriched in Sm, relative to Nd, compared to the chondritic average; (2) the Earth was constructed largely from materials enriched in *s*- and/or *p*-process isotopes (Carlson et al., 2007; Gannoun et al., 2011); (3) a low Sm/Nd reservoir with negative μ^{142}Nd formed early in the Earth or in precursor materials and was isolated (Boyet and Carlson, 2005; Labrosse et al., 2007) or collisionally eroded away (Caro et al., 2006; O'Neill and Palme, 2008).

Options (1) and (2) may be unlikely because those primitive materials are rare. Additionally, nucleosynthetic heterogeneity may not be sufficient to account for the offset (i.e., Carlson et al., 2007; Caro, 2011; Gannoun et al., 2011; Qin et al., 2011). Consequently, here we quantitatively explore whether option (3) is a viable process in light of the observed μ^{142}Nd and μ^{182}W variations in observed in early Earth rocks, but consider the consequences of (1) and (2).

1.2. Processes that control μ^{142}Nd and μ^{182}W after the Earth accreted

Variations in μ^{142}Nd can only be produced by crystal-liquid fractionation in the silicate Earth within the lifetime of ^{146}Sm; (1) and (2) from above cannot lead to variations in ^{142}Nd after accretion. However, additional processes must be considered as possible causes for ^{182}W variations in the mantle, such as:

1. Addition of late accreted materials with bulk chondritic compositions (μ^{182}W $\sim$ -200) to the mantle.
2. Addition of a core component (μ^{182}W $\sim$ -220) to the mantle.
3. Merging of a differentiated impactor's mantle with Earth's mantle.
4. Metal-silicate equilibration, while ^{182}Hf was extant, resulting in variable modification of Hf/W in the mantle during core-segregation.
5. Crystal - liquid fractionation in the silicate Earth occurring while ^{182}Hf was extant by either:
    (a) Partial melting of the mantle;
    (b) Magma ocean differentiation.

Late accretion and core-mantle interactions (processes 1 and 2) would cause the μ^{182}W value of normal mantle to decrease. A core-merging giant impact (process 3) could also potentially cause the μ^{182}W of the mantle to increase, but such a high-energy impact would also likely result in a new partial or full magma ocean (Rubie et al., 2011), which would then homogenize the initial, now potentially higher, Hf/W composition of the liquid mantle. Process 4, metal-silicate equilibration at high temperatures and pressures, was proposed by Touboul et al. (2012) as a means of establishing a high Hf/W reservoir in the lower mantle that would evolve to a higher μ^{182}W than overlying mantle. This reservoir could contribute W with high μ^{182}W to a plume rising from the deep mantle. However, none of these processes (1, 2, 3 or 4) influence Sm/Nd or ^{142}Nd. Thus, only process 5 has the potential to explain the variability in both systems as a result of a single process.

Early partial melting (process 5a) can potentially account for local isotopic anomalies (e.g., Touboul et al., 2012), but it cannot likely account for the global ^{142}Nd chondritic offset unless an early formed proto-crust was subducted and preserved (e.g., Chase and Patchett, 1988; Tolstikhin and Hofmann, 2005). However, if it is possible to isolate a proto-crust, then it may also be possible that a dense, enriched magma ocean residue was isolated. Therefore, in this paper we explore a scenario in which it is possible to explain both the offset in ^{142}Nd from the chondritic average and early Earth isotopic variability with process 5b. As will be shown by our modeling, the crystallization of a terrestrial magma ocean, followed by overturn (process 5b) can produce the observed isotopic variability of both ^{142}Nd and ^{182}W, as well as account for the apparent ^{142}Nd offset from the chondritic average. Our model also explores both the effects of the putative Moon-forming giant impact onto the Earth, after ^{182}Hf was no longer extant (Touboul et al., 2007), and modest late accretion (~0.3-0.8 wt% of Earth's mass) following the giant impact.

Our holistic approach towards dealing with the two short-lived systems does not preclude the other processes from also occurring, potentially obscuring any early record of process 5b. For example, process 4 could explain the variations in μ^{182}W, but it may be difficult to distinguish this process from process 5. Process 3 could result in the increase of Hf/W in a partial or full magma ocean, compared to the previous mantle. If this event occurred while ^{182}Hf was still extant, subsequent crystallization (process 5b) could create ^{182}W variability. If this event instead occurred after ^{182}Hf was no longer extant, crystallization could result in variable μ^{142}Nd but uniform, excess μ^{182}W. Furthermore, if (1) or (2) is the cause of the terrestrial ^{142}Nd chondritic average offset, process 5b could still explain early Earth variability. Thus, the preserved short-lived isotopic record in early Earth rocks and early Solar System materials was most likely generated by a combination of the mechanisms discussed above.

1.3. Considerations of the ^{147}Sm-^{143}Nd system

The ^{147}Sm-^{143}Nd (half-life=106 Gyr) serves as an important complement to the short-lived ^{146}Sm-^{142}Nd system when considering early Earth evolution. The best estimate of the ϵ^{143}Nd (where ϵ^{143}Nd is the deviation in the $\frac{^{143}\mathrm{Nd}}{^{144}\mathrm{Nd}}$ ratio from that of the chondritic average in parts per 10,000) composition of the accessible depleted mantle today derives from the relatively narrow composition of the MORB source region: 10±2 (e.g., Bennett, 2003). Thus, any realistic depleted reservoir that could explain μ^{142}Nd observations must retain those characteristics, plus the additional depletion caused by the extraction of the continental crust. While long-term complex magmatic differentiation precludes matching specific ^{143}Nd compositions of early Earth rocks in our model, we require successful model simulations to lie within the known parameters of Earth's Nd composition.

Other long-lived systems (e.g., Os, Pb, Xe) might also be considered with respect to large-scale early Earth evolutionary processes, but are beyond the scope of this study. For example, the long-lived ^{176}Hf system behaves similarly to that of the ^{143}Nd system in low pressure environments, but may behave quite differently, due to perovskite fractionation in a magma ocean (e.g., Kato et al., 1988; Walter and Tronnes, 2004; Jackson et al., 2014).

2. Methods

2.1. Modeling early mantle differentiation (Process 5b) constrained by ^{142}Nd, ^{143}Nd, and ^{182}W

Invoking a Hadean magma ocean to account for the ∼20 ppm offset in μ^{142}Nd between the bulk silicate Earth and the chondritic average requires that a minimum of two reservoirs form: a small early enriched reservoir (EER, using the terminology of Carlson and Boyet (2008)), characterized by high concentrations of incompatible elements and sub-chondritic Sm/Nd, and a large complementary early depleted reservoir (EDR, using the terminology of Boyet and Carlson (2006) and Carlson and Boyet (2008)), characterized by comparatively low concentrations of incompatible elements, and slightly supra-chondritic Sm/Nd. As a result of the greater incompatibility of W, compared to Hf, in most silicate igneous systems, the EER would most likely also be characterized by sub-chondritic Hf/W, and the EDR would be characterized by supra-chondritic Hf/W. With time the EER would evolve to negative μ^{142}Nd, ϵ^{143}Nd, and μ^{182}W values, while the EDR would evolve to zero or positive μ^{142}Nd, ϵ^{143}Nd, and μ^{182}W values.

While formation of unmixed EERs and EDRs can explain the μ^{142}Nd difference between the chondritic average and the accessible Earth and could account for a major portion of the ϵ^{143}Nd enrichment observed in the convecting mantle today, this process alone fails to account for the observed early Earth isotopic variability in ^{142}Nd and ^{182}W; subsequent igneous processes would be required (i.e., process 5a). However, if there was partial mixing of the newly formed EER back into the EDR, the EDR would evolve in isotopic composition proportional to the mixing rate, and thus, could potentially also produce the early Earth isotopic variability (Carlson and Boyet, 2008; Willbold et al., 2011; Touboul et al., 2012).

Partial-mixing of the EER back into the depleted reservoir would likely have occurred gradually (Blichert-Toft and Puchtel, 2010; Rizo et al., 2012), and so the mantle at any given time would have contained regions with more or less of the enriched component. Therefore, in this model the primary mantle source region of the Isua, Kostomuskha, and Nuvvuagittuq rocks is either pure or relatively unmixed initial EDR. The Komati komatiites, sans isotopic anomalies, would then be derived from a region of the mantle that had been more efficiently mixed with the EER. If (1) or (2) is shown to be the cause of the ^{142}Nd chondritic average offset, then full mixing of the EDR and EER by the time μ^{142}Nd isotopic heterogeneities disappeared (presently 2.7 Ga, Figure 1) could explain the variability. Thus, there are three types of post-overturn mixing models (mixing-absent, partial-mixing, and full-mixing) which can explain the ^{142}Nd chondritic average offset and/or short-lived isotopic variability. Such processes would also have led to isotopic heterogeneities in the ^{143}Nd isotopic composition of the mantle. However, imprecision in our knowledge of the evolution of ^{143}Nd in the mantle during early Earth history means this system can contribute only minimally to constraining the nature of these possible processes.

To accurately model this process, crystallization sequences and mineral-melt partition coefficients for Sm, Nd, Hf, and W must be known. However, partition coefficients are mostly unconstrained for mantle phases crystallizing from an early terrestrial magma ocean. In addition to the limited availability of appropriate partition coefficients, fO_2 and pressure can strongly affect partition coefficients, yet these intensive parameters for a global magma ocean are also poorly constrained. Therefore, because of the paucity of relevant partitioning data, and the complexity of the system, a modified Monte Carlo technique is used to vary Hf, W, Sm, Nd partition coefficients in a crystallizing magma ocean to model the trace element evolution of potential reservoirs formed in the early Earth. Utilizing a single invariant partition coefficient is a simplifying assumption supported by the fact that Sm/Nd and Hf/W ratios are more insensitive to external conditions than the individual partition coefficients, and elemental ratios are most critical to isotopic variability.

2.2. The magma ocean model

2.2.1. Terrestrial magma ocean solidification

In our model, the young Earth is assumed to have been partially to wholly molten, due to the combined heat released from accretion, core formation, and decay of radiogenic isotopes (Solomatov, 2000, 2007). To simplify modeling, a single magma ocean event is assumed, even though this is unlikely. The implications of serial full or partial magma oceans are discussed in Section 4.3.

The resulting magma ocean solidification proceeds in two stages. In the first stage, as the magma ocean cools, crystals initially form near the core (Solomatov, 2000, 2007; Elkins-Tanton, 2008). Fractional crystallization continues, which leads to continual enrichment of the magma ocean liquid in dense iron and other dense incompatible elements, producing a mantle that evolves to increasing Fe concentration and density towards the surface (Hess and Parmentier, 1995). In the second stage of magma ocean solidification, this gravitationally unstable solid mantle overturns and reorganizes so that the mantle density decreases towards the surface, resulting in dense, late stage magma ocean cumulates residing near the core-mantle boundary (Solomatov, 2000; Elkins-Tanton et al., 2003, 2005a,b; Elkins-Tanton, 2008). This mechanism that brings dense, enriched cumulates to the base of the mantle can potentially account for the seismologically observable large low-shear velocity provinces (LLSVPs) (Trampert et al., 2004), regardless of how cumulate reservoirs may have mixed after the magma ocean solidified.

While there is increasing evidence that terrestrial magma ocean solidification may not have proceeded from the bottom (Stixrude et al., 2009), assuming simple fractional solidification does not substantively change the results of our model. Even if fractionation proceeded in two regions simultaneously, the densest final cumulates (the EER) from the upper magma ocean would sink through the intervening mantle and join the last fractionates of the lower magma ocean (Elkins-Tanton, 2008). Similarly, a partial-mantle magma ocean or even serial magma oceans would likely still result in a gravitationally stable mantle with the final, most dense cumulates (the EER) sinking towards the core-mantle boundary (Elkins-Tanton, 2012).

Crystallization of a global magma ocean is modeled using code for Earth from Elkins-Tanton (2008). The code requires *a priori* knowledge of the equilibrium mineral phases and proportions; the assumed phases used in this paper are given in Figure 2. The magma ocean code either retains 1% or 5% interstitial liquid in cumulates; these percentages are arbitrary and were chosen to assess how the results are influenced by varying this parameter.

The bulk composition (Table 1) of the mantle used for the model described here is the Hart and Zindler (1986) Earth composition for major oxides. Compositions for the trace elements Sm, Nd and Hf are from McDonough and Sun (1995) and W is from Arevalo and McDonough (2008).

2.2.2. Partition Coefficients

Given that relevant partition coefficients of Sm, Nd, Hf, and W in deep mantle mineral phases are not well constrained, this study explores their likely range by using a modified Monte Carlo approach to consider possible combinations of coefficients in the magma ocean code. Using the Geochemical Earth Reference Model database (`http://earthref.org/KDD/`), a database was created of all measured, calculated or experimentally determined partition coefficient pairs of Sm-Nd and Hf-W in compositional systems appropriate for a terrestrial magma ocean (Table 2).

The published range in partition coefficients for a given trace element in a mineral is very large, typically on the order of 2-4 orders of magnitude, depending on conditions such as temperature, pressure and composition of the system. By contrast, the partition coefficient ratios for two trace elements in a mineral are predictive and typically vary by no more than one order of magnitude or less. Using this useful constraint, a modified Monte Carlo method was developed to avoid exploring the full, unrealistic, parameter space for individual elements, because it is both presently intractable and would not predict a physically reasonable set of successful partition coefficients. For example, the same model was run with an unmodified Monte Carlo approach (constrained only by individual partition coefficients) and out of 20,000 simulations, only 5 conformed to reasonable partition coefficient ratios (Table 2) among orthopyroxene, clinopyroxene, and garnet, and only one produced a "successful" result (defined in Table 3). This is a misleading conclusion (i.e., it is misleading that only 1 out of 20,000 (0.005%) simulations can explain observed isotopic compositions) because only 5 out of the 20,000 simulations were physically reasonable. The more appropriate conclusion would be that 1 out of 5 (20%) simulations could explain observed isotopic compositions.

Thus, this algorithm relies on knowing the range of viable melt-mineral partition coefficients for each element-element-mineral pair, from which the range of reasonable ratios of these partition coefficients within a mineral can be calculated. We assume, but cannot verify, that the data we use from the literature reasonably approximate the true natural values, if they could be known.

For each iteration a partition coefficient (PC1) from the database, for a given element in a given mineral, is randomly chosen as a reference. The difference (d) is calculated by subtracting the chosen partition coefficient and the next closest partition coefficient. If there are 5 or fewer paired entries for a mineral in the database, the difference (d) between the two partition coefficients is doubled to account for the likely too narrowly defined range of possible values. Then a partition coefficient for the model simulation is randomly chosen within the space PC1±d. The same process is done to choose a partition coefficient ratio (PC1/PC2), which allows calculation of the remaining partition coefficient value (PC2) to be used, as long as it is within its respective PC2±d space, in the crystallization code. This method allows us to fill in and also expand the parameter space slightly, while conforming to the known range of coefficients.

If there are one or no Sm-Nd or Hf-W partition coefficient pairs known for a given mineral, then a different approach to estimating reasonable ranges is needed (Table 2 denotes these as "guesses"). Few partition coefficients exist for W, so estimates for that system are guided by the fact that in the silicate Earth W behaves similarly to U (Righter and Shearer, 2003; Arevalo and McDonough, 2008, and references therein). Additionally, for many minerals the Hf/W partition coefficient ratio is always greater than 1 (e.g., Touboul et al., 2012); however, U can be more compatible than Hf in calcium perovskite, and thus, we allow the Hf/W ratio to be less than 1. For the crystallization code, reasonable maximum PC1 (e.g., Hf) and PC2 (e.g., W) partition coefficients and minimum and maximum PC1/PC2 (e.g., Hf/W) partition coefficient ratios are estimated. Then random numbers are generated between 0 and the PC1 or PC2 maximum partition coefficient, and between the minimum and maximum PC1/PC2 partition coefficient ratios. Table 2 reports the bounds of the database and the estimates used in the algorithm. The full database and the algorithm can be made available upon request.

2.3. Converting Monte Carlo magma ocean simulations to potential early Earth reservoirs

After completion of the Monte Carlo simulations, the next step is to define the mixing-absent and partial-mixing reservoirs (Section 2.3.1), isotopically evolve them (Section 2.3.2), and determine if they are successful (Table 3). We do not explicitly calculate the full-mixing scenario (Section 2.1) because it is computationally prohibitive to model different Sm and Nd initial concentrations, but we can extrapolate the results of the mixing-absent and partial-mixing scenarios to this case.

2.3.1. Defining the EER and the EDR

For each simulation, the magma ocean code calculates the concentration of Hf, W, Nd, and Sm in cumulates and in residual liquid before and after overturn, as a function of radius within the Earth. Since only the trace element concentrations change between simulations, the density profile and subsequent overturn stratigraphy of mineral phases are not changed between the Monte Carlo simulations.

The magma ocean code predicts a finely layered and highly heterogeneous cumulate mantle immediately following solidification. To model the EER, we mix a varying thickness of the lower mantle into a homogeneous composition, as shown as R1-5 and O1-5 in Figure 2. Using these possible EERs and EDRs (the remaining cumulate mantle), we are able to test whether they explain both the global deviations from the chondritic μ^{142}Nd average, and excess μ^{142}Nd and μ^{182}W in early Earth rocks (illustrated in (Figure 2)). Regardless of mixing, any EER that could potentially explain the isotopic anomalies must have lower Hf/W and Sm/Nd ratios, but be more concentrated in incompatible elements, than the EDR. For example in the Hf-W system the constraints are: $(\frac{\mathrm{Hf}}{\mathrm{W}})_{\mathrm{EDR}} > (\frac{\mathrm{Hf}}{\mathrm{W}})_{\mathrm{EER}}$, $\mathrm{Hf}_{\mathrm{EDR}} < \mathrm{Hf}_{\mathrm{EER}}$ and $\mathrm{W}_{\mathrm{EDR}} < \mathrm{W}_{\mathrm{EER}}$.

Thus, to immediately remove obvious failures, the Hf/W and the Sm/Nd ratios of each possible EDR and EER pair for each simulation (shown as R1-5 and O1-5 in Figure 2) are calculated for both the mixing-absent and the partial-mixing models. In the mixing-absent model, the EER is defined as the lowermost 2 vol% of the mantle, consistent with seismic observations of the LLSVPs (Williams and Garnero, 1996; Garnero, 2000; Berryman, 2000; Burke et al., 2008; Garnero and McNamara, 2008; Hernlund and Houser, 2008, and references therein). In the partial-mixing model, the EDR-EER transition is then defined as either the maximum or the minimum EER thickness that has smaller Hf/W and Sm/Nd ratios, but is more concentrated in Sm, Nd, Hf, and W than the EDR. If for a particular simulation there is no thickness that allows the EER to have lower elemental ratios than the EDR, or if there is a larger concentration of incompatible elements in the EDR, then that simulation is considered a failure.

2.3.2. Decay to present day measurable rocks

The ratios of Hf/W and Sm/Nd of the possible EDRs and EERs are used, along with known initial Solar System isotopic ratios, to calculate the radioactive decay of reservoirs to their present day values for comparison with the anomalous early Earth rocks. Initial Solar System isotopic ratios are given in Supplementary Table 2. To compute the isotopic evolution, $^{142}\mathrm{Nd}/^{144}\mathrm{Nd}$ and $^{182}\mathrm{W}/^{184}\mathrm{W}$ (assuming chondritic Hf/W and Sm/Nd) ratios are first mathematically evolved from the time of accretion until the time of an unknown core-formation / mantle differentiation event. The uncertainty in the timing of core-formation and mantle differentiation, which were likely not simultaneous and also progressive rather than occurring during a single event, influences the eventual W and Nd isotopic composition of the entire mantle. For ease of computation, post mantle-differentiation reservoir evolution was calculated every 1 Myr between 1-100 Myr after Solar System formation (~4.567 Ga (Amelin et al., 2010)). Then the decay of the EDR and EER was calculated from the mantle-differentiation event to the present using the Hf/W and Sm/Nd compositions from the magma ocean code. A delay between core-formation and mantle differentiation would result in greater ^{182}W anomalies (Moynier et al., 2010).

For the partial-mixing model, the EDR post-mixing (hereafter called the Depleted Accessible Earth, after the terminology in the supplementary information of Willbold et al. (2011)) μ^{182}W or μ^{142}Nd is calculated by:

$$\mu^{182}\mathrm{W} \text{ or } \mu^{142}\mathrm{Nd} = \frac{\mathrm{C_D}\mu_\mathrm{D}(1-\mathrm{X}) + \mathrm{C_E}\mu_\mathrm{E}\mathrm{X}}{\mathrm{C_D}(1-\mathrm{X}) + \mathrm{C_E}\mathrm{X}}, \tag{1}$$

where X is the percent of the EER reservoir mixed into the EDR, $\mathrm{C_E}$ is the wt% of W or Nd in the EER, μ_E is the isotopic composition μ^{182}W or μ^{142}Nd of the EER, $\mathrm{C_D}$ is the wt% of W or Nd in the EDR, and μ_D is the isotopic composition μ^{182}W or μ^{142}Nd of the EDR. Constraints for isotopically successful simulations are given in Table 3.

3. Model Results

The statistics of the simulation results are given in Table 4 and illustrated in Figure 3. Successful individual and ratio partition coefficients are given in Table 5, and the compositions of the late stage liquids are given in Table 1.

3.1. Major elements

Previous studies have considered early Earth differentiation and its effect on chondritic major element ratios (e.g., Kato et al., 1988; Walter and Tronnes, 2004; Walter et al., 2004). One product of the model presented here is the major element composition of the Depleted Accessible Earth. The volume of the LLSVP is so small that the major element bulk composition of the Depleted Accessible Earth changes by a maximum of +0.2wt% for SiO_2, +0.1wt% for Al_2O_3, -0.7wt% for FeO, +0.5wt% for MgO, and 0.0 wt% for CaO, and so is effectively unresolvable from the bulk silicate Earth starting composition. The CaO/Al_2O_3 in the Depleted Accessible Mantle predicted by the model is lower than needed to explain the Earth's apparent superchondritic CaO/Al_2O_3, but the model does not include changes in Ca and Al content of pyroxenes, majorite, and perovskite that might change the model trend, and so we conclude that our model is not sufficiently tuned to Ca and Al to answer this question.

3.2. $\mu^{182}W$

Simulations are first judged on whether they produce, based on volume and density considerations, a deep, overturned EER and shallower EDR (Section 2.3.1). Simulations that do not produce that mantle geometry are discarded. Among all the model variants, 54-83% of simulations fail in this way. Simulations are more likely to produce the correct EDR-EER configuration if they contain more interstitial liquid and / or have an isolated EER that never mixes. Of the remaining simulations, 100% of the late accretion and late giant impact and 34-68% of no late accretion model variants can, at least once during the calculated time of differentiation, produce the observed isotopic anomalies. Among all the model variants, the 5% interstitial liquid, late accretion model has the maximum percentage of successful isotopic simulations. Combined, model variants are isotopically successful between 24-68 Myr with peaks between 31-47 Myr (Figure 3B). Successful EDRs range in μ^{182}W from -5 to +1723 ppm and successful EERs range in μ^{182}W from -178 to +233 ppm.

The window in time that produces successful simulations is sensitive to both the initial concentration of W in the bulk magma ocean, the amount of interstitial liquid retained in cumulates, and the extent of mixing of the EER into the EDR. The reason why no simulations are successful prior to 24 Myr is because isotopic anomalies are generally too large in magnitude to ever evolve to the modern day isotopic composition; thus, if there is more W initially in the silicate Earth, the magnitude of anomalies are damped, shifting the window earlier in time. When more liquid is trapped, late stage liquids are less enriched and less fractionated, and do not evolve isotopic excesses for as long ($\sim$14 Myr), facilitating a high Hf/W EDR and lower μ^{182}W EDR. Regardless, the Depleted Accessible Earth can be obtained using the known range of partition coefficients, and is not sensitive to which layers may have comprised the EER.

The range of partition coefficients in successful simulations is the same as the range of partition coefficients from the literature (Table 2). The most striking result is that the Hf partition coefficient in Mg-perovskite needs to be < 2 (Supplementary Figure 5). This is because Hf is otherwise too compatible, resulting in $\mathrm{Hf_{EDR}} > \mathrm{Hf_{EER}}$.

3.3. $\mu^{142}Nd$

Among all the model variants, 9-32% of simulations fail to produce a deep overturned EER and shallow EDR, and are thus discarded. Here again simulations are more often successful with more interstitial liquid and/or an isolated EER that never mixes; 0.8 - 20% of simulations are isotopically successful. Simulations are successful between 1 and >100 Myr with peaks between 1 and 40 Myr (Figure 3A). Isotopic successes are more successful with higher amounts of retained interstitial liquid and an unmixed EER. However, between the minimum and maximum mixing models, the maximum mixing model is significantly more successful and suggests the Sm-Nd system is more sensitive to this than the Hf-W system.

Successful EDRs range in μ^{142}Nd from -5 to +122 ppm, and successful EERs range in μ^{142}Nd from -210 to +2 ppm. The ϵ^{143}Nd composition of the Depleted Accessible Earth ranges between 5 and 12, which suggests that to have isolated a reservoir to the present day requires a nonchondritic Sm/Nd ratio of the Depleted Accessible Earth. Successful simulations extend roughly 10 Myr or more later (Figure 3) when the longer half-life of ^{146}Sm, 103 Myr, (Kinoshita et al., 2012) is used. Partition coefficients used in isotopically successful simulations generally fall within the range given by the database (Supplementary Figure 4).

4. Discussion

The results of this study suggest that solidification of the Earth from a magma ocean inevitably produces a heterogeneous mantle, which can be simplified as depleted and enriched reservoirs. No mixing is required between the depleted and enriched reservoirs to explain the deviation from the chondritic ^{142}Nd average; however, to explain the isotopic variability observed in early Earth rocks, partial-mixing of the EER back into the EDR is required. While we did not numerically investigate the scenario in which the offset from chondritic ^{142}Nd was entirely a product of nucleosynthetic heterogeneity, our results suggest that in that case, early Earth short-lived isotopic variability could have been generated during the eventual complete mixing of the EER back into the EDR (i.e., a fully-mixed model instead of an unmixed or partially-mixed model).

Successful simulations correlate with greater amounts of interstitial liquid trapped in cumulates and, if configured appropriately, thicker initial EERs. Using the longer half-life of ^{146}Sm (103 Myr) causes the distribution of successful simulations in the Sm-Nd system to shift later in time by 10 Myr or more. Both isotopic systems are generally insensitive to the type of mixing model assumed, even in the case of a giant impact followed by late accretion, however maximum mixing and no mixing are preferred. Successful simulations suggest mantle differentiation could have occurred between the minimum range of 24-68 Myr after Solar System formation. This window shifts to earlier times if more W is assumed for the bulk silicate Earth composition. Indeed, if a partial-mixing model is likely, then the concentration of incompatible elements in the silicate mantle would be underestimated (i.e., the concentration used here and in Willbold et al. (2011), taken from Arevalo and McDonough (2008), would be too low).

Below, application of the model to a more realistic, complex early Earth history is addressed by discussing inefficient overturn, the likelihood of mixing and stability of enriched reservoirs, and the effects of giant impacts and multiple magma oceans.

4.1. Inefficient overturn

Numerical modeling of lunar, mercurian, and martian mantle overturn (Elkins-Tanton et al., 2002; Brown and Elkins-Tanton, 2012; Scheinberg et al., 2014) suggests that overturn will not be 100% efficient because the coldest, most viscous material near the surface might form a stiff crust resistant to foundering. On Earth, the higher gravity, abundance of water, and differences in mineralogy may encourage foundering and eliminate any remnant first crust. If inefficient overturn is viable on Earth, however, material at the core-mantle boundary and at the surface may both become re-entrained by mantle convection. This mechanism may prove vital to explaining how early Earth rocks sampled the enriched reservoir; however, a separate differentiation event within the lifetime of ^{146}Sm could also explain the enriched μ^{142}Nd compositions (Rizo et al., 2012, 2013). The results of our mixing model are indistinguishable from this more complex model of inefficient overturn.

4.2. Stability of the EER

We have only one constraint on the timescale of mixing: the youngest date of ^{142}Nd or ^{182}W variable rocks. Currently, that is 2.7 Ga (Figure 1); future work may push this date to later times. This indicates that mixing of a heterogeneous post-overturned, crystallized magma ocean should take at least 1.8 Ga, but after this minimum duration very little enriched material (less than 10-20% (Andreasen et al., 2008)) can be allowed to be entrained into the Depleted Accessible Earth. Various studies have attempted to quantify how long heterogeneities can persist, which depends on numerous variables including the density / composition, viscosity, temperature, heat flux, and thickness of a hidden reservoir (e.g., Davies, 1984; Sleep, 1988; Manga, 1996; Farnetani, 1997; Becker et al., 1999; Davaille, 1999; Jellinek and Manga, 2002; Bourdon and Caro, 2007; Manga, 2010; Li et al., 2014). These studies are encouraging, and suggest that dense material can have long lifetimes (up to 40 Gyr). However, more research is required to specifically examine the details of the model discussed here to address the efficiency of overturn and the nature of compositional layers convecting and homogenizing post-overturn.

Even without numerical models, insight into the stability of the EER after overturn can be gained using simple calculations. After overturn, the temperature of the compositionally dense EER is cooler than that of the overlying, compositionally lighter EDR mantle. Eventually this temperature profile will invert due to core heating and radioactive decay, allowing for convective heat loss as hot material near the core-mantle boundary becomes buoyant. However, if the material near the core-mantle boundary is so dense that, even heated, it will not overcome the overlying compositional density, it will not participate in mantle convection. The density of the EER, if heated to a temperature similar to that of the EDR, can then be calculated and compared to the overlying density. The temperature of the most dense layer in the EDR as a reference was chosen here because it is the most likely material to become more dense than the EER. Figure 4 shows the calculated results, and suggests entrainment of the top portion of the EER due to its low density contrast with the overlying EDR. Perhaps a more realistic mixing scenario is one in which overturned cumulates above the most dense, enriched material slowly mixes into the overlying EDR while the deepest EER material remains isolated.

The very bottom of the EER will likely melt from radiogenic heating, but because the melt will be more dense than its surroundings (Ohtani and Maeda, 2001; Stixrude and Karki, 2005; Mosenfelder et al., 2007), it will remain near the core-mantle boundary, consistent with seismologically observed partial melt in the D" (Williams and Garnero, 1996; Garnero, 2000; Berryman, 2000; Hernlund and Houser, 2008; Hier-Majumder, 2008). Based on high pressure experiments, Thomas et al. (2012) found that while a pyrolite melt would not be dense enough to remain at the core-mantle boundary, a partial melt with a relatively high-iron liquid content would be gravitationally dense and stable. In our model, the liquids produced by partial melting of the iron and incompatible element enriched layers would certainly fall within the range of liquid compositions stable in the ultra low velocity zone (ULVZ), found as their Figure 10 in Thomas et al. (2012).

Furthermore, the density of the EER in our models (10-20% greater than that of the EDR) is comparable to the density contrasts expected for the LLVSPs (a few percent (e.g., Garnero and McNamara, 2008)) and the ULVZ (10$\pm$5% (Rost et al., 2005)). While our model densities are slightly high if the EER is the entire set of LLVSPs, the error associated with the density of the final cumulates and liquids is likely the cause of this discrepancy. Also, the LLVSPs may be home to more compositions (e.g., enriched recycled crust, core-mantle chemical boundary layer) than enriched magma ocean cumulates (e.g., Deschamps et al., 2012; Peto et al., 2013).

4.3. Multiple partial magma oceans

Giant impacts are a critical part of terrestrial planet formation, which suggests that the Earth likely experienced multiple full or partial magma oceans (e.g., Tucker and Mukhopadhyay, 2014). Regardless of timing, if a successive impact only partially melted the mantle, the magma ocean would again crystallize and overturn, producing cumulates with a range of Hf/W and Sm/Nd ratios shifted relative to previous events depending on both the extent of melting and the mass and composition of the impactor in the melt. If this event occurred during the lifetime of ^{182}Hf, cumulates would have variable μ^{182}W and μ^{142}Nd, which would then either mix or remain isolated.

If crystallization occurred after ^{182}Hf was extinct, cumulates would only evolve isotopic variations in μ^{142}Nd and not μ^{182}W. The overturned, uniform μ^{182}W partial-mantle would then need to gradually mix with μ^{182}W-variable unremelted cumulates to explain early Earth variability. Interestingly, serial magma oceans could help explain μ^{182}W-μ^{142}Nd decoupling. Isotopic analyses of lunar rocks may suggest a late, successive impact; there is a range of reported μ^{142}Nd consistent with expected partitioning behavior (i.e., KREEP has negative μ^{142}Nd while low-titanium mare basalts have positive μ^{142}Nd (Nyquist et al., 1995; Boyet and Carlson, 2007; Brandon et al., 2009) but no resolvable variation in μ^{182}W (Touboul et al., 2009)). Additionally, some lunar formation models would likely lead to incomplete melting and mixing of the mantle (Solomatov, 2000; Ćuk and Stewart, 2012), suggesting that a late giant impact would therefore be consistent with the time window given by our model (Figure 3).

5. Conclusion

It is possible to match seismic observations of the LLVSPs, early variable ^{142}Nd and ^{182}W measurements, and the ^{142}Nd difference between the accessible Earth and average ordinary chondrites utilizing the magma ocean reservoir hypothesis (Carlson and Boyet, 2008) constrained by the ^{147}Sm-^{143}Nd system, and a known set of Sm, Nd, Hf, and W partition coefficients. Our results also indicate that an unmixed EER-EDR scenario (i.e., early Earth isotopic variability was generated by very early partial melting) or a fully-mixed EDR-EER scenario (i.e., terrestrial ^{142}Nd was produced by nucleosynthetic heterogeneity) are also viable models to explain, respectively, the remaining terrestrial deviation from chondritic ^{142}Nd and early Earth ^{142}Nd and ^{182}W variability.

Both isotopic systems indicate that the most likely time to successfully explain all the isotopic measurements considered here is $\sim$40 Myr after Solar System formation, but this peak would shift earlier as more W is included in the initial bulk composition. Simulations that fail isotopically have calculated excess μ^{142}Nd and μ^{182}W Depleted Accessible Earth compositions too high to match modern observations, suggesting that magma ocean differentiation inevitably produces isotopic reservoirs; the challenge is damping their excess and depleted compositions. Short-lived isotopic systems suggest that mantle mixing was sluggish, incomplete, and heterogeneous during at least the first $\sim$1.8 Ga of Earth history (Figure 1), and hint that negative μ^{182}W anomalies could be preserved somewhere on Earth.

Acknowledgements

This work was supported by NSF CSEDI grants EAR1265169 to RJW, EAR1160656 to LTET, and NASA grant NNX12AH80G to TLG. We extend our gratitude to Timothy Grove, Alexandra Andrews, Ann Bauer, and Benjamin Mandler for helpful discussion and to Christopher Reeder for helpful discussion about algorithms. We graciously thank Maud Boyet and two anonymous reviewers for their thoughtful comments and questions, which improved this paper.

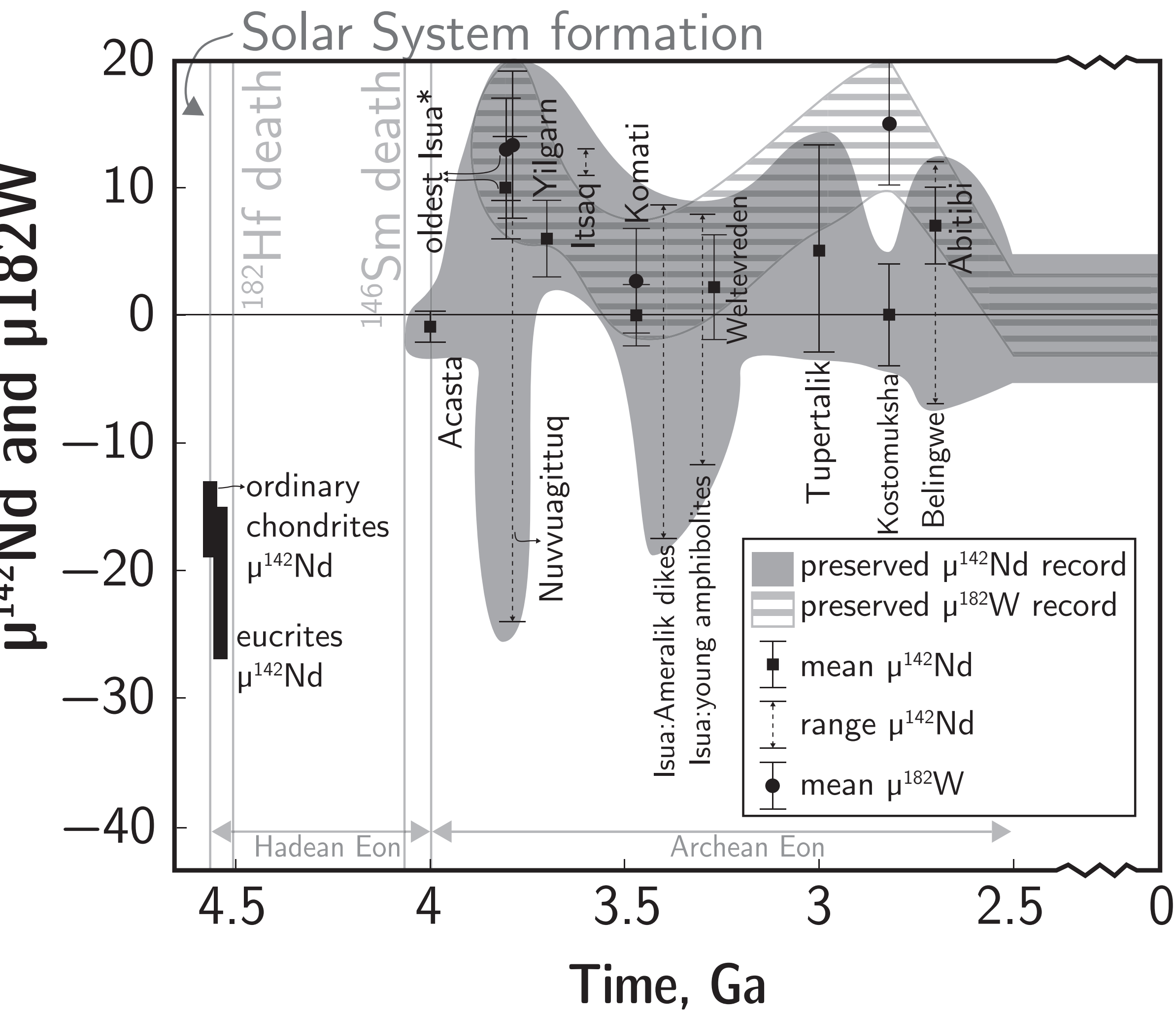

Figure 1 : Compilation of presently available short-lived radioisotopic signatures preserved in the rock record. If reported, a location-based average isotopic anomaly is plotted. Otherwise, a dashed line is plotted to span the range of data for a specific location.*The oldest Isua data are plotted slightly offset from the 3.8 Ga date to clearly distinguish the data from the Nuvvuagittuq data. The oldest Isua data are from Willbold et al. (2011) and Caro et al. (2006) because they report both μ^{142}Nd and μ^{182}W for the same Isua rock samples. However, the extended range reported by many other studies in similar and nearby rocks (e.g. the oldest Istaq complex samples from Bennett et al. (2007)), up to +20 ppm, is reflected in the grey shading of μ^{142}Nd (the full compilation is given by Rizo et al. (2013). Data are from Caro et al. (2006); Boyet and Carlson (2006); Bennett et al. (2007); Carlson and Boyet (2008); Willbold et al. (2011); O'Neil et al. (2012); Rizo et al. (2012); Touboul et al. (2012, 2014); Puchtel et al. (2013); Rizo et al. (2013); Debaille et al. (2013). Chondrite and eucrite range taken from Carlson and Boyet (2008). The 68 Myr half-life of ^{146}Sm was used by (Rizo et al., 2013) to calculate a 3.3 Ga Lu-Hf / Sm-Nd age of Isua: young amphibolites (the corresponding U-Pb age is 3.01 Ga). All other ages were determined using U-Pb, Pb-Pb, or Re-Os systematics. The Nuvvuagittuq data are plotted using the zircon date.

Table 1 : Magma ocean bulk composition in wt % unless noted otherwise. Major elements are from Hart and Zindler (1986). Sm, Nd, and Hf are from McDonough and Sun (1995) and W is from Arevalo and McDonough (2008). H_2O and CO_2 are not listed, but the code was run with 0.5% H_2O and 0.1% CO_2. Range of major element compositions of late stage liquids (LSL) are reported with 1% - 5% interstitial liquid retained in cumulates. Trace element compositions of late stage liquids are taken from all successful modified Monte Carlo simulations listed in Table 4.

	SiO_2	Al_2O_3	FeO	MgO	CaO	Sm(ppm)	Nd(ppm)	Hf(ppm)	W(ppb)
bulk magma ocean	46.6	4.1	7.6	38.3	3.2	0.41	1.25	0.28	13
90% LSL	41.9-42.4	2.6-2.9	22-23.4	28.8-29.4	3.3-3.4	0.30 - 3.3	1.6 - 10	0.12 - 2.2	53 - 126
95% LSL	37.5-38.6	3.0-3.5	31.9-34.8	19.8-21.1	4.9-5	0.39 - 6.0	2.4 - 19	0.063 - 4.3	97 - 253
98% LSL	30.6-32.4	3.4-4.4	45.5-48.8	6.9-7.6	10.2	0.41 - 14	3.8 - 44	0.025 - 11	215 - 652
99% LSL	26.5-30.2	3.2-4.9	47.5-52.8	3.1-4.1	13.2-14.4	0.41 - 18	4.3 - 57	0.018 - 14	279 - 886

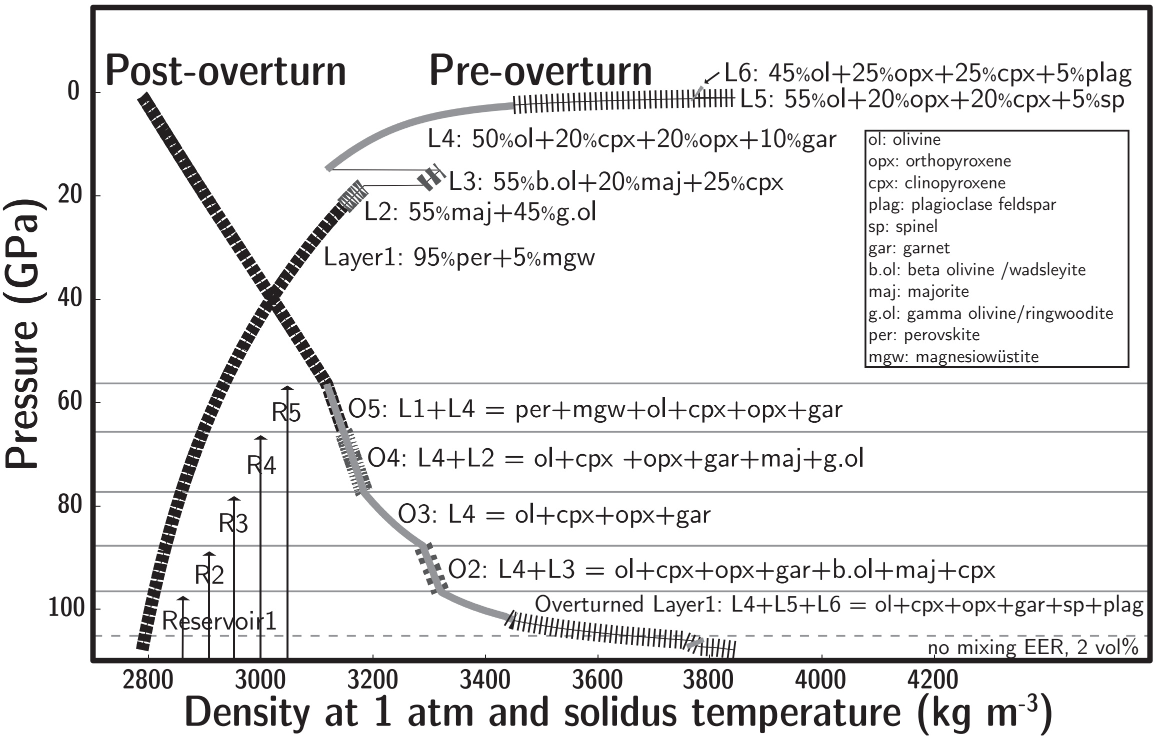

Figure 2 : Density of the mantle pre- and post-overturn calculated at 1 atm and the solidus temperature; the density of high pressure phases (perovskite, magnesiowustite, majorite, wadsleyite, ringwoodite) was recalculated for lower pressure phases. After overturn, new layers (denoted as “O”) can be mixtures of old layers (denoted as “L”) based on density, producing an azimuthally heterogeneous mantle. The possible EER regions discussed through the paper are shown as R1 - R5. The post-overturn layers are then recalculated based on stable mineral assemblages, but are compositionally the same as the mineralogy of the pre-overturn layers.

Table 2 : Range of partition coefficients and ratios for Sm, Nd, Hf, W in mantle mineral phases that control the isotopic composition of Earth reservoirs. This set of available data is used to reflect the viable parameter space for the constrained Monte Carlo simulations. References refer to minimum and maximum values reported or all references used to guide a guess.

	Sm Range	Nd Range	Sm/Nd Range	# of pairs	References
olivine	0.00012 - 0.362	0.000029 - 0.355	0.66 - 8.3	31	Shimizu et al. (1982); Mibe et al. (2006); Larsen (1979); Adam and Green (2006); McKay (1986)
wadsleyite	0 - 0.01	0 - 0.01	1 - 100	guess	Mibe et al. (2006)
ringwoodite	0 - 0.01	0 - 0.01	1 - 100	guess	
clinopyroxene	0.067 - 4.3	0.039 - 3.06	0.97 - 2.75	129	Salters and Longhi (1999); Nagasawa (1973); Shimizu (1980); Fujimaki et al. (1984)
orthopyroxene	0.0016 - 0.064	0.00049 - 0.065	0.925 - 3.27	24	Kennedy et al. (1993)
garnet	0.053 - 1.1	0.016 - 0.73	0.94 - 7.39	56	Mibe et al. (2006); Hauri et al. (1994); Irving and Frey (1978); McKENZIE and O'NIONS (1991); Green et al. (2000)
majorite	0.048 - 0.12	0.013 - 0.04	2.0 - 9.2	6	Walter et al. (2004); Corgne and Wood (2004); Corgne et al. (2012)
plagioclase	0.009- 6.816	0.014 - 3.2	0.085 - 6.4	61	McKay et al. (1994); Bindeman et al. (1998); Dunn and Sen (1994); Bindeman and Davis (2000)
spinel	0.01 - 0.18	0.01 - 0.24	0.75 - 1	2	Elkins et al. (2008); McKENZIE and O'NIONS (1991)
Mg-perovskite	0.04 - 0.16	0.015 - 0.08	1.5 - 3.12	12	Corgne et al. (2005); Liebske et al. (2005)
Ca-perovskite	8.4 - 23	6.7 - 18	1.19 - 1.28	6	Corgne et al. (2005)
Mg-wustite/periclase	0 - 0.01	0 - 0.01	1 - 50	guess	Walter et al. (2004)
	Hf Range	**W Range**	**Hf/W Range**	**# of pairs**	
olivine	0.0008 - 0.07	0.0001 - 0.07	1 - 40	3	Shearer (2003); Adam and Green (2006)
wadsleyite	0 - 0.01	0 - 0.01	1 - 100	guess	Mibe et al. (2006)
ringwoodite	0 - 0.01	0 - 0.01	1 - 100	guess	
clinopyroxene	0.04 - 6.27	0.00014 - 0.33	0.12 - 15675	18	Shearer (2003); Hill et al. (2000); Adam and Green (2006)
orthopyroxene	0.0111 - 0.15	0.00018 - 0.015	5.3 - 105	9	Klemme et al. (2006); Sun and Liang (2013); Shearer (2003)
garnet	0.06 - 0.52	0.0007 - 0.01	20 - 173	5	Adam and Green (2006); Shearer (2003)
majorite	0 - 0.3	0 - 0.1	1 - 50	guess	Corgne et al. (2012)
plagioclase	0.064 - 0.27	0.062 - 0.25	0.18 - 2.25	7	Luhr et al. (1984); Lee (1997); Touboul et al. (2009)
spinel	0 - 1	0 - 0.1	1 - 50	guess	Klemme et al. (2006)
Mg-perovskite	0 - 3	0 - 0.5	1 - 100	guess	Corgne et al. (2005); Liebske et al. (2005); Touboul et al. (2012)
Ca-perovskite	0 - 3	0 - 3	0.5 - 50	guess	Corgne et al. (2005); Corgne and Wood (2005); Touboul et al. (2012)
Mg-wustite/periclase	0 - 0.01	0 - 0.01	1 - 50	guess	

Table 3 : Isotopic requirements for successful Monte Carlo simulations. In the case of the mixing-absent model variant, the EER = DAE and model constraints are given by the DAE. EDR = Early Depleted Reservoir, EER = Early Enriched Reservoir, DAE = Depleted Accessible Earth

	μ^{142}Nd	ϵ^{143}Nd	μ^{182}W *No Late Accretion*	μ^{182}W *Late Accretion*	μ^{182}W *Late Giant Impact*
EDR	≥20±3.5 Bennett et al. (2007)	-	≥15±4.8 Touboul et al. (2012)	≥15±4.8 Touboul et al. (2012)	≥15±4.8 Touboul et al. (2012)
DAE	0±5	0 - 12 estimated from Bennett (2003); Carlson and Boyet (2008); Willbold et al. (2011)	0±5	10±5 - 30±5 Willbold et al. (2011)	195−235 Halliday (2008)

Table 4 : Summary of terrestrial magma ocean model results for the 15,000 Monte Carlo simulations. IL = interstitial liquid percent, A = veneer model where LA = late accretion, NLA = no late accretion, LGI = late giant impact (constraint in Table 3 includes additional late accretion), F = obvious failed simulations, S = isotopically successful simulations, TW = successful timing window in Myr, TWP = peak of successful timing window in Myr, %STWP = percent of isotopically successful simulations at the TWP (Figure 3), EDR = EDR isotopic compositional range of successful simulations, EER = EER isotopic compositional range of successful simulations.

IL	EER definition	A	$t_{\frac{1}{2}}$ (^{146}Sm)	% F	% S	TW	TWP	% STWP	EDR	EER
Hf-W									μ^{182}W	μ^{182}W
1%	min	LA	-	83	100	32-67	45	13	10 - 161	-167 - 34
1%	max	LA	-	83	100	32-66	45	14	10 - 836	-167 - 34
1%	mixing-absent	LA	-	71	100	33-66	44	15	5-35	-178 - 33
5%	min	LA	-	63	100	33-53	40	23	10 - 117	-170 - 34
5%	max	LA	-	63	100	32-52	40	23	10 - 523	-170 - 34
5%	mixing-absent	LA	-	54	100	33-53	40	23	5-35	-177-34
1%	min	NLA	-	83	34	34-68	47	3	10 - 115	-169 - -16
1%	max	NLA	-	83	36	34-67	46	3	10 - 688	-169 - -4
1%	mixing-absent	NLA	-	71	66	34-67	43	7	-5 - 5	-179 - 4
5%	min	NLA	-	63	39	36-54	43	5	10 - 69	-172 - -23
5%	max	NLA	-	63	46	34-52	43	6	10 - 420	-172 - -3
5%	mixing-absent	NLA	-	54	68	34-54	41	9	-5 - 5	-178 - 4
1%	min	LGI	-	83	100	24-59	35	10	196 - 476	-147 - 231
1%	max	LGI	-	83	100	24-57	35	10	196 - 1723	-147 - 231
1%	mixing-absent	LGI	-	71	100	24-57	35	11	195-235	-165 - 233
5%	min	LGI	-	63	100	24-45	31-32	16	195 - 383	-152 - 232
5%	max	LGI	-	63	100	24-43	32	16	195 - 1140	-153 - 233
5%	mixing-absent	LGI	-	54	100	24-44	32	16	195-235	-163 - 232
Sm-Nd									μ^{142}Nd	μ^{142}Nd
1%	min	-	68	32	2.6	1-67	10-40	0.8	17 - 42	-176 - -30
1%	max	-	68	32	6.8	1-97	40	5	17 - 122	-135 - -4
1%	mixing-absent	-	68	18	11	1-97	40	10	-5-5	-210 - 2
5%	min	-	68	20	1.3	1-47	10-30	0.3	17 - 25	-181 - -28
5%	max	-	68	20	11	1-96	40	8	17 - 105	-110 - -3
5%	mixing-absent	-	68	9	20	1-97	40	18	-5 - 5	-205 - 1
1%	min	-	103	32	2.0	1-77	1-40	0.8	17 - 34	-153 - -30
1%	max	-	103	32	6.4	1-100+	37	5	17 - 114	-95 - -4
1%	mixing-absent	-	103	18	11	1-100+	38	10	-5-5	-182 - 2
5%	min	-	103	20	0.8	1-47	1-30	0.3	17 - 25	-154 - -28
5%	max	-	103	20	11	1-100+	37	8	17 - 105	-99 - -3
5%	mixing-absent	-	103	9	20	1-100+	37	18	-5 - 5	-179 - 1

Table 5 : Range of successful partition coefficients between all model variants for Sm, Nd, Hf, W for mantle mineral phases that control the isotopic composition of Earth reservoirs.

	Sm		Nd		Sm/Nd	
	minimum	maximum	minimum	maximum	minimum	maximum
olivine	0.0000037	0.40	0.00000063	0.36	0.58	9.6
wadsleyite	0.00019	0.010	0.000026	0.0099	1.0	94
ringwoodite	0.000048	0.010	0.0000086	0.0097	1.0	100
clinopyroxene	0.065	4.8	0.040	3.1	0.90	2.7
othropyroxene	0.0016	0.069	0.00047	0.069	0.87	3.5
garnet	0.031	1.1	0.012	1.0	0.68	7.8
majorite	0.0080	0.16	0.00079	0.058	0.65	19
plagioclase	0.0051	9.1	0.014	3.7	0.037	10
spinel	0.00023	0.52	0.00017	0.70	0.25	1.5
Mg-perovskite	0.034	0.17	0.014	0.086	1.2	3.2
Ca-perovskite	0.6	27	0.51	22	1.2	1.3
Mg-wustite	0.00077	0.10	0.00014	0.099	1.0	50

	Hf		W		Hf/W	
	minimum	maximum	minimum	maximum	minimum	maximum
olivine	0.0000010	0.20	0.000000010	0.21	0.0032	110
wadsleyite	0.000096	0.010	0.0000072	0.010	1.0	95
ringwoodite	0.00011	0.010	0.0000063	0.0098	1.0	99
clinopyroxene	0.00067	9.4	0.00013	0.36	0.19	21000
othropyroxene	0.00098	0.29	0.00014	0.036	0.43	140
garnet	0.000035	0.94	0.00000022	0.010	3.4	210
majorite	0.0013	0.30	0.00067	0.10	1.0	50
plagioclase	0.0029	0.36	0.035	0.30	0.040	2.8
spinel	0.0043	1.0	0.00075	0.10	1.0	50
Mg-perovskite	0.032	2.0	0.0020	0.50	1.0	99
Ca-perovskite	0.020	3.0	0.0077	3.0	0.50	50
Mg-wustite	0.0011	0.10	0.00022	0.10	1.0	50

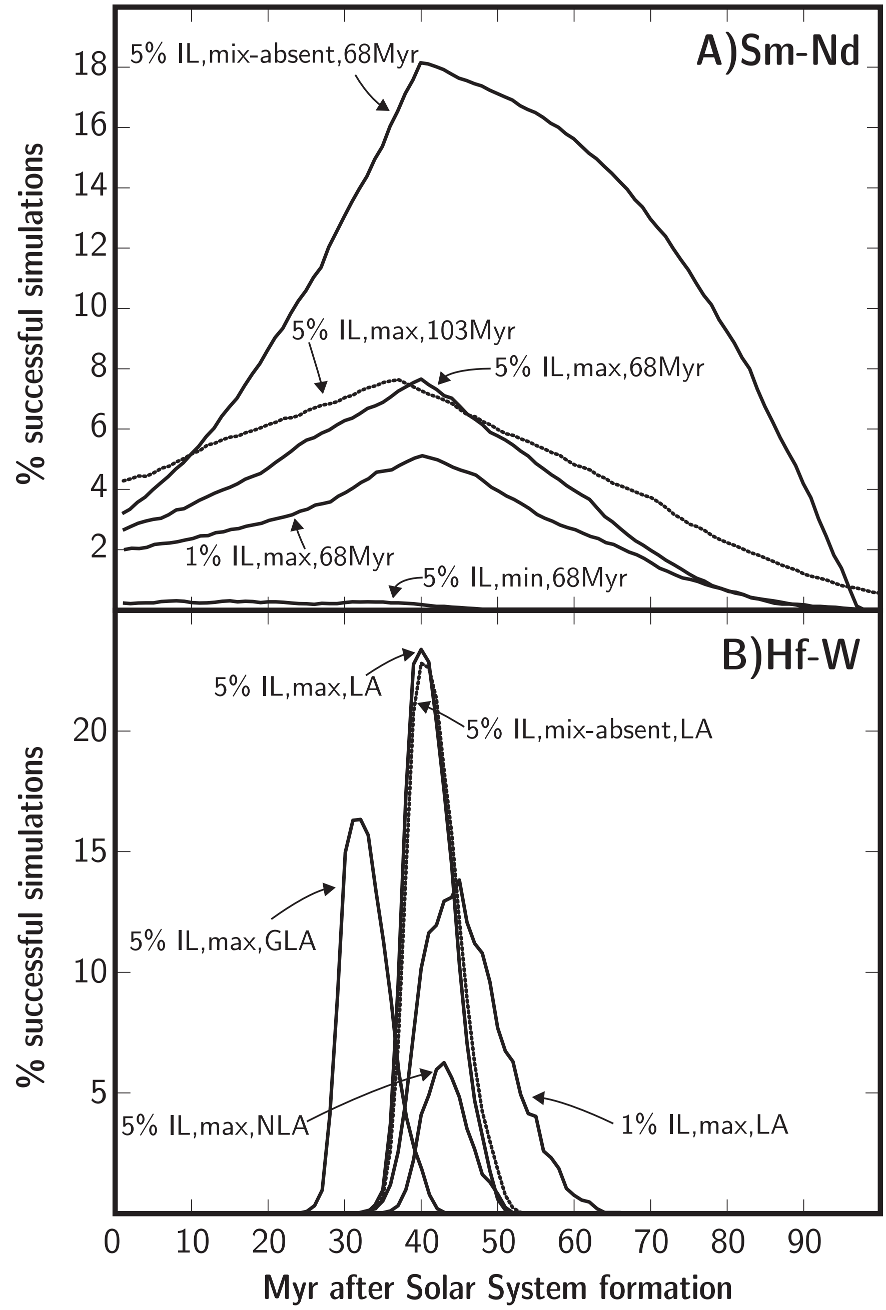

Figure 3 : Successful simulations are sensitive to when the Earth differentiated. Abbreviations are given in Table 4. The percentage of successful simulations also depends on the amount of interstitial liquid (indicated as 1% or 5% IL, where IL = interstitial liquid) retained in cumulates, the mixing model (i.e. how the early enriched reservoir is defined: min, max, or mixing-absent), and the half-life of ^{146}Sm (indicated as 68 or 103 Myr). For both systems, the peak extends to later times with lower percent interstitial liquid retained in cumulates. Both systems also show little variation between mixing models (but the Sm-Nd is more sensitive) when the same IL% and either the same late accretion scenario or same ^{146}Sm half-life is assumed. A) Behavior of the Sm-Nd system. The shorter half-life causes the curve to extend ~10 Myr or more later. B) Behavior of the Hf-W system. The percentage is lowest for the case in which the mantle μ^{182}W was not drawdown by late accretion (NLA).

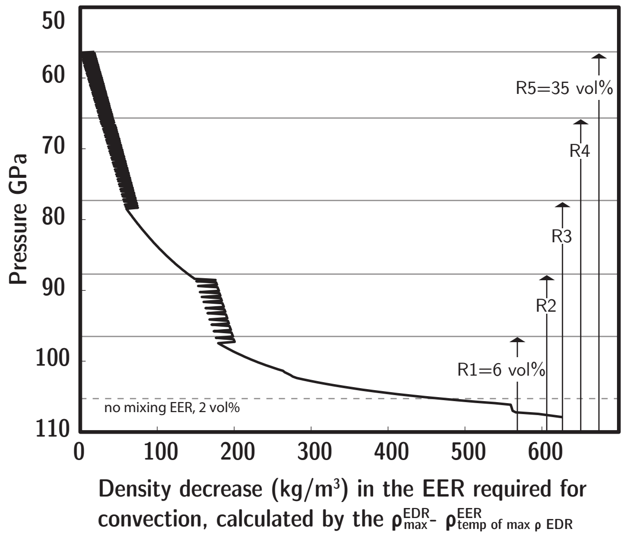

Figure 4 : The shallowest potential enriched material is likely to be entrained and mixed when mantle convection turns on, suggesting that the partial-mixing model is likely. The deepest enriched material is extremely dense, and even melted, would not become buoyant (Mosenfelder et al., 2007; Thomas et al., 2012, and references therein). How long mixing will take is unknown, but would need to extend to ~2.7 Ga (Figure 1) to explain measured isotopic variability.

References

Adam, J., Green, T., 2006. Trace element partitioning between mica- and amphibole-bearing garnet lherzolite and hydrous basanitic melt: 1. Experimental results and the investigation of controls on partitioning behaviour. Contributions to Mineralogy and Petrology 152, 1–17.

Amelin, Y., Kaltenbach, A., Iizuka, T., Stirling, C.H., Ireland, T.R., Petaev, M., Jacobsen, S.B., 2010. UPb chronology of the Solar System's oldest solids with variable 238U/235U. Earth and Planetary Science Letters 300, 343–350.

Andreasen, R., Sharma, M., Subbarao, K., Viladkar, S., 2008. Where on Earth is the enriched Hadean reservoir? Earth and Planetary Science Letters 266, 14–28.

Arevalo, R., McDonough, W.F., 2008. Tungsten geochemistry and implications for understanding the Earth's interior. Earth and Planetary Science Letters 272, 656–665.

Becker, T.W., Kellogg, J.B., O'Connell, R.J., 1999. Thermal constraints on the survival of primitive blobs in the lower mantle. Earth and Planetary Science Letters 171, 351–365.

Bennett, V.C., 2003. Compositional Evolution of the Mantle. Treatise on Geochemistry 2, 493–519.

Bennett, V.C., Brandon, A.D., Nutman, A.P., 2007. Coupled 142Nd-143Nd isotopic evidence for Hadean mantle dynamics. Science 318, 1907–10.

Berryman, J.G., 2000. Seismic velocity decrement ratios for regions of partial melt in the lower mantle. Geophysical Research Letters 27, 421–424.

Bindeman, I.N., Davis, A.M., 2000. Trace element partitioning between plagioclase and melt: investigation of dopant influence on partition behavior. Geochimica et Cosmochimica Acta 64, 2863–2878.

Bindeman, I.N., Davis, A.M., Drake, M.J., 1998. Ion Microprobe Study of Plagioclase-Basalt Partition Experiments at Natural Concentration Levels of Trace Elements. Geochimica et Cosmochimica Acta 62, 1175–1193.

Blichert-Toft, J., Puchtel, I.S., 2010. Depleted mantle sources through time: Evidence from LuHf and SmNd isotope systematics of Archean komatiites. Earth and Planetary Science Letters 297, 598–606.

Bourdon, B., Caro, G., 2007. The early terrestrial crust. Comptes Rendus Geoscience 339, 928–936.

Boyet, M., Carlson, R., 2006. A new geochemical model for the Earth's mantle inferred from 146Sm142Nd systematics. Earth and Planetary Science Letters 250, 254–268.

Boyet, M., Carlson, R.W., 2005. 142Nd evidence for early (4.53 Ga) global differentiation of the silicate Earth. Science 309, 576–81.

Boyet, M., Carlson, R.W., 2007. A highly depleted moon or a non-magma ocean origin for the lunar crust? Earth and Planetary Science Letters 262, 505–516.

Brandon, A.D., Lapen, T.J., Debaille, V., Beard, B.L., Rankenburg, K., Neal, C., 2009. Re-evaluating 142Nd/144Nd in lunar mare basalts with implications for the early evolution and bulk Sm/Nd of the Moon. Geochimica et Cosmochimica Acta 73, 6421–6445.

Brown, S., Elkins-Tanton, L., 2012. The Early Dynamics and Density Structure of Mercury's Mantle. Lunar and Planetary Science Conference 2062.

Burke, K., Steinberger, B., Torsvik, T.H., Smethurst, M.a., 2008. Plume Generation Zones at the margins of Large Low Shear Velocity Provinces on the coremantle boundary. Earth and Planetary Science Letters 265, 49–60.

Carlson, R.W., Boyet, M., 2008. Composition of the Earth's interior: the importance of early events. Phil. Trans. R. Soc. A 366, 4077–103.

Carlson, R.W., Boyet, M., Horan, M., 2007. Chondrite barium, neodymium, and samarium isotopic heterogeneity and early Earth differentiation. Science 316, 1175–8.
Caro, G., 2011. Early Silicate Earth Differentiation. Annual Review of Earth and Planetary Sciences 39, 31–58.
Caro, G., Bourdon, B., Birck, J.l., Moorbath, S., 2003. 146Sm-142Nd evidence from Isua metamorphosed sediments for early differentiation of the Earth's mantle. Nature 423, 428–32.
Caro, G., Bourdon, B., Birck, J.L., Moorbath, S., 2006. High-precision 142Nd/144Nd measurements in terrestrial rocks: Constraints on the early differentiation of the Earths mantle. Geochimica et Cosmochimica Acta 70, 164–191.
Chase, C., Patchett, P., 1988. Stored mafic/ultramafic crust and early Archean mantle depletion. Earth and Planetary Science Letters 91, 66–72.
Corgne, A., Armstrong, L.S., Keshav, S., Fei, Y., McDonough, W.F., Minarik, W.G., Moreno, K., 2012. Trace element partitioning between majoritic garnet and silicate melt at 1017GPa: Implications for deep mantle processes. Lithos 148, 128–141.
Corgne, A., Liebske, C., Wood, B.J., Rubie, D.C., Frost, D.J., 2005. Silicate perovskite-melt partitioning of trace elements and geochemical signature of a deep perovskitic reservoir. Geochimica et Cosmochimica Acta 69, 485–496.
Corgne, A., Wood, B.J., 2004. Trace element partitioning between majoritic garnet and silicate melt at 25GPa. Physics of the Earth and Planetary Interiors 143-144, 407–419.
Corgne, A., Wood, B.J., 2005. Trace element partitioning and substitution mechanisms in calcium perovskites. Contributions to Mineralogy and Petrology 149, 85–97.
Ćuk, M., Stewart, S.T., 2012. Making the Moon from a fast-spinning Earth: a giant impact followed by resonant despinning. Science (New York, N.Y.) 338, 1047–52.
Davaille, A., 1999. Simultaneous generation of hotspots and superswells by convection in a heterogeneous planetary mantle. Nature 402, 756–760.
Davies, G.F., 1984. Geophysical and isotopic constraints on mantle convection: An interim synthesis. Journal of Geophysical Research 89, 6017.
Debaille, V., O'Neill, C., Brandon, A.D., Haenecour, P., Yin, Q.Z., Mattielli, N., Treiman, A.H., 2013. Stagnant-lid tectonics in early Earth revealed by 142Nd variations in late Archean rocks. Earth and Planetary Science Letters 373, 83–92.
Deschamps, F., Cobden, L., Tackley, P.J., 2012. The primitive nature of large low shear-wave velocity provinces. Earth and Planetary Science Letters 349-350, 198–208.
Dunn, T., Sen, C., 1994. Mineral/matrix partition coefficients for orthopyroxene, plagioclase, and olivine in basaltic to andesitic systems: A combined analytical and experimental study. Geochimica et Cosmochimica Acta 58, 717–733.
Elkins, L., Gaetani, G., Sims, K., 2008. Partitioning of U and Th during garnet pyroxenite partial melting: Constraints on the source of alkaline ocean island basalts. Earth and Planetary Science Letters 265, 270–286.
Elkins-Tanton, L., 2008. Linked magma ocean solidification and atmospheric growth for Earth and Mars. Earth and Planetary Science Letters 271, 181–191.
Elkins-Tanton, L., Zaranek, S., Parmentier, E., Hess, P., 2005a. Early magnetic field and magmatic activity on Mars from magma ocean cumulate overturn. Earth and Planetary Science Letters 236, 1–12.

Elkins-Tanton, L.T., 2012. Magma Oceans in the Inner Solar System. Annual Review of Earth and Planetary Sciences 40, 113–139.
Elkins-Tanton, L.T., Hess, P.C., Parmentier, E.M., 2005b. Possible formation of ancient crust on Mars through magma ocean processes. Journal of Geophysical Research 110, E12S01.
Elkins-Tanton, L.T., Parmentier, E.M., Hess, P.C., 2003. Magma ocean fractional crystallization and cumulate overturn in terrestrial planets: Implications for Mars. Meteoritics & Planetary Science 38, 1753–1771.
Elkins-Tanton, L.T., Van Orman, J.A., Hager, B.H., Grove, T.L., 2002. Re-examination of the lunar magma ocean cumulate overturn hypothesis: melting or mixing is required. Earth and Planetary Science Letters 196, 239–249.
Farnetani, C.G., 1997. Excess temperature of mantle plumes: The role of chemical stratification across D. Geophysical Research Letters 24, 1583–1586.
Fujimaki, H., Tatsumoto, M., Aoki, K.i., 1984. Partition coefficients of Hf, Zr, and ree between phenocrysts and groundmasses. Journal of Geophysical Research 89, B662.
Gannoun, A., Boyet, M., Rizo, H., El Goresy, A., 2011. 146Sm-142Nd systematics measured in enstatite chondrites reveals a heterogeneous distribution of 142Nd in the solar nebula. Proceedings of the National Academy of Sciences of the United States of America 108, 7693–7.
Garnero, E.J., 2000. Heterogeneity of the Lowermost Mantle. Annual Review of Earth and Planetary Sciences 28, 509–537.
Garnero, E.J., McNamara, A.K., 2008. Structure and dynamics of Earth's lower mantle. Science 320, 626–8.
Green, T., Blundy, J., Adam, J., Yaxley, G., 2000. SIMS determination of trace element partition coefficients between garnet, clinopyroxene and hydrous basaltic liquids at 27.5 GPa and 10801200C. Lithos 53, 165–187.
Halliday, A.N., 2008. A young Moon-forming giant impact at 70-110 million years accompanied by late-stage mixing, core formation and degassing of the Earth. Philosophical transactions. Series A, Mathematical, physical, and engineering sciences 366, 4163–81.
Hart, S.R., Zindler, A., 1986. In search of a bulk-earth composition. Chemical Geology 57, 247–267.
Hauri, E.H., Wagner, T.P., Grove, T.L., 1994. Experimental and natural partitioning of Th, U, Pb and other trace elements between garnet, clinopyroxene and basaltic melts. Chemical Geology 117, 149–166.
Hernlund, J.W., Houser, C., 2008. On the statistical distribution of seismic velocities in Earth's deep mantle. Earth and Planetary Science Letters 265, 423–437.
Hess, P., Parmentier, E., 1995. A model for the thermal and chemical evolution of the Moon's interior: implications for the onset of mare volcanism. Earth and Planetary Science Letters 134, 501–514.
Hier-Majumder, S., 2008. Influence of contiguity on seismic velocities of partially molten aggregates. Journal of Geophysical Research 113, B12205.
Hill, E., Wood, B.J., Blundy, J.D., 2000. The effect of Ca-Tschermaks component on trace element partitioning between clinopyroxene and silicate melt. Lithos 53, 203–215.
Irving, A.J., Frey, F.A., 1978. Distribution of trace elements between garnet megacrysts and host volcanic liquids of kimberlitic to rhyolitic composition. Geochimica et Cosmochimica Acta 42, 771–787.
Jackson, C.R., Ziegler, L.B., Zhang, H., Jackson, M.G., Stegman, D.R., 2014. A geochemical evaluation of potential magma ocean dynamics using a parameterized model for perovskite crystallization. Earth and Planetary Science Letters 392, 154–165.

Jellinek, A.M., Manga, M., 2002. The influence of a chemical boundary layer on the fixity, spacing and lifetime of mantle plumes. Nature 418, 760–763.

Kato, T., Ringwood, A., Irifune, T., 1988. Experimental determination of element partitioning between silicate perovskites, garnets and liquids: constraints on early differentiation of the mantle. Earth and Planetary Science Letters 89, 123–145.

Kennedy, A., Lofgren, G., Wasserburg, G., 1993. An experimental study of trace element partitioning between olivine, orthopyroxene and melt in chondrules: equilibrium values and kinetic effects. Earth and Planetary Science Letters 115, 177–195.

Kinoshita, N., Paul, M., Kashiv, Y., Collon, P., Deibel, C.M., DiGiovine, B., Greene, J.P., Henderson, D.J., Jiang, C.L., Marley, S.T., Nakanishi, T., Pardo, R.C., Rehm, K.E., Robertson, D., Scott, R., Schmitt, C., Tang, X.D., Vondrasek, R., Yokoyama, a., 2012. A Shorter 146Sm Half-Life Measured and Implications for 146Sm-142Nd Chronology in the Solar System. Science 335, 1614–1617.

Klemme, S., Günther, D., Hametner, K., Prowatke, S., Zack, T., 2006. The partitioning of trace elements between ilmenite, ulvospinel, armalcolite and silicate melts with implications for the early differentiation of the moon. Chemical Geology 234, 251–263.

Labrosse, S., Hernlund, J.W., Coltice, N., 2007. A crystallizing dense magma ocean at the base of the Earth's mantle. Nature 450, 866–9.

Larsen, L.M., 1979. Distribution of REE and other trace elements between phenocrysts and peralkaline undersaturated magmas, exemplified by rocks from the Gardar igneous province, south Greenland. Lithos 12, 303–315.

Lee, D., 1997. Age and Origin of the Moon. Science 278, 1098–1103.

Li, Y., Deschamps, F., Tackley, P.J., 2014. The stability and structure of primordial reservoirs in the lower mantle: insights from models of thermochemical convection in three-dimensional spherical geometry. Geophysical Journal International 199, 914–930.

Liebske, C., Corgne, A., Frost, D.J., Rubie, D.C., Wood, B.J., 2005. Compositional effects on element partitioning between Mg-silicate perovskite and silicate melts. Contributions to Mineralogy and Petrology 149, 113–128.

Luhr, J.F., Carmichael, I.S., Varekamp, J.C., 1984. The 1982 eruptions of El Chichón Volcano, Chiapas, Mexico: Mineralogy and petrology of the anhydrite-bearing pumices. Journal of Volcanology and Geothermal Research 23, 69–108.

Manga, M., 1996. Mixing of heterogeneities in the mantle: Effect of viscosity differences. Geophysical Research Letters 23, 403–406.

Manga, M., 2010. Low-viscosity mantle blobs are sampled preferentially at regions of surface divergence and stirred rapidly into the mantle. Physics of the Earth and Planetary Interiors 180, 104–107.

McDonough, W., Sun, S.s., 1995. The composition of the Earth. Chemical Geology 120, 223–253.

McKay, G., Le, L., Wagstaff, J., Crozaz, G., 1994. Experimental partitioning of rare earth elements and strontium: Constraints on petrogenesis and redox conditions during crystallization of Antarctic angrite Lewis Cliff 86010. Geochimica et Cosmochimica Acta 58, 2911–2919.

McKay, G.A., 1986. Crystal/liquid partitioning of REE in basaltic systems: Extreme fractionation of REE in olivine. Geochimica et Cosmochimica Acta 50, 69–79.

McKENZIE, D., O'NIONS, R.K., 1991. Partial Melt Distributions from Inversion of Rare Earth Element Concentrations. Journal of Petrology 32, 1021–1091.

Mibe, K., Orihashi, Y., Nakai, S., Fujii, T., 2006. Element partitioning between

transition-zone minerals and ultramafic melt under hydrous conditions. Geophysical Research Letters 33, L16307.
Mosenfelder, J.L., Asimow, P.D., Ahrens, T.J., 2007. Thermodynamic properties of Mg 2 SiO 4 liquid at ultra-high pressures from shock measurements to 200 GPa on forsterite and wadsleyite. Journal of Geophysical Research 112, B06208.
Moynier, F., Yin, Q.z., Irisawa, K., Boyet, M., Jacobsen, B., Rosing, M.T., 2010. Coupled 182W-142Nd constraint for early Earth differentiation. Proceedings of the National Academy of Sciences of the United States of America 107, 10810–4.
Nagasawa, H., 1973. Rare-earth distribution in alkali rocks from Oki-Dogo Island, Japan. Contributions to Mineralogy and Petrology 39, 301–308.
Nyquist, L., Wiesmann, H., Bansal, B., Shih, C.Y., Keith, J., Harper, C., 1995. 146Sm-142Nd formation interval for the lunar mantle. Geochimica et Cosmochimica Acta 59, 2817–2837.
Ohtani, E., Maeda, M., 2001. Density of basaltic melt at high pressure and stability of the melt at the base of the lower mantle. Earth and Planetary Science Letters 193, 69–75.
O'Neil, J., Carlson, R.W., Francis, D., Stevenson, R.K., 2008. Neodymium-142 evidence for Hadean mafic crust. Science (New York, N.Y.) 321, 1828–31.
O'Neil, J., Carlson, R.W., Paquette, J.L., Francis, D., 2012. Formation age and metamorphic history of the Nuvvuagittuq Greenstone Belt. Precambrian Research 220-221, 23–44.
O'Neill, H.S.C., Palme, H., 2008. Collisional erosion and the non-chondritic composition of the terrestrial planets. Philosophical transactions. Series A, Mathematical, physical, and engineering sciences 366, 4205–38.
Peto, M.K., Mukhopadhyay, S., Kelley, K.a., 2013. Heterogeneities from the first 100 million years recorded in deep mantle noble gases from the Northern Lau Back-arc Basin. Earth and Planetary Science Letters 369-370, 13–23.
Puchtel, I., Blichert-Toft, J., Touboul, M., Walker, R., Byerly, G., Nisbet, E., Anhaeusser, C., 2013. Insights into early Earth from Barberton komatiites: Evidence from lithophile isotope and trace element systematics. Geochimica et Cosmochimica Acta 108, 63–90.
Qin, L., Carlson, R.W., Alexander, C.M., 2011. Correlated nucleosynthetic isotopic variability in Cr, Sr, Ba, Sm, Nd and Hf in Murchison and QUE 97008. Geochimica et Cosmochimica Acta 75, 7806–7828.
Righter, K., Shearer, C., 2003. Magmatic fractionation of Hf and W: constraints on the timing of core formation and differentiation in the Moon and Mars. Geochimica et Cosmochimica Acta 67, 2497–2507.
Rizo, H., Boyet, M., Blichert-Toft, J., O'Neil, J., Rosing, M.T., Paquette, J.L., 2012. The elusive Hadean enriched reservoir revealed by 142Nd deficits in Isua Archaean rocks. Nature 491, 96–100.
Rizo, H., Boyet, M., Blichert-Toft, J., Rosing, M.T., 2013. Early mantle dynamics inferred from 142Nd variations in Archean rocks from southwest Greenland. Earth and Planetary Science Letters 377-378, 324–335.
Rost, S., Garnero, E.J., Williams, Q., Manga, M., 2005. Seismological constraints on a possible plume root at the core-mantle boundary. Nature 435, 666–9.
Rubie, D.C., Frost, D.J., Mann, U., Asahara, Y., Nimmo, F., Tsuno, K., Kegler, P., Holzheid, A., Palme, H., 2011. Heterogeneous accretion, composition and coremantle differentiation of the Earth. Earth and Planetary Science Letters 301, 31–42.
Salters, V.J., Longhi, J., 1999. Trace element partitioning during the initial stages of melting beneath mid-ocean ridges. Earth and Planetary Science Letters 166, 15–30.
Scheinberg, A., Elkins-Tanton, L.T., Zhong, S.J., 2014. Timescale and morphology

of Martian mantle overturn immediately following magma ocean solidification. Journal of Geophysical Research: Planets 119, 454–467.

Shearer, C.K., 2003. Behavior of tungsten and hafnium in silicates: A crystal chemical basis for understanding the early evolution of the terrestrial planets. Geophysical Research Letters 30, 1007.

Shimizu, H., 1980. Experimental study on rare-earth element partitioning in minerals formed at 20 and 30kb for basaltic systems. Geochem. J 14, 185–202.

Shimizu, H., Sangen, K., Masuda, A., 1982. Experimental study on rare-earth element partitioning in olivine and clinopyroxene formed at 10 and 20kb for basaltic systems. Geochemical Journal 16, 107–117.

Sleep, N.H., 1988. Gradual entrainment of a chemical layer at the base of the mantle by overlying convection. Geophysical Journal International 95, 437–447.

Solomatov, V., 2000. Fluid dynamics of a terrestrial magma ocean. Origin of the Earth and Moon , 323–338.

Solomatov, V., 2007. Magma Oceans and Primordial Mantle Differentiation. Treatise on geophysics 9, 91–119.

Stixrude, L., Karki, B., 2005. Structure and freezing of MgSiO3 liquid in Earth's lower mantle. Science 310, 297–9.

Stixrude, L., de Koker, N., Sun, N., Mookherjee, M., Karki, B.B., 2009. Thermodynamics of silicate liquids in the deep Earth. Earth and Planetary Science Letters 278, 226–232.

Sun, C., Liang, Y., 2013. Distribution of REE and HFSE between low-Ca pyroxene and lunar picritic melts around multiple saturation points. Geochimica et Cosmochimica Acta 119, 340–358.

Thomas, C.W., Liu, Q., Agee, C.B., Asimow, P.D., Lange, R.A., 2012. Multi-technique equation of state for Fe2SiO4 melt and the density of Fe-bearing silicate melts from 0 to 161 GPa. Journal of Geophysical Research 117, B10206.

Tolstikhin, I., Hofmann, A.W., 2005. Early crust on top of the Earth's core. Physics of the Earth and Planetary Interiors 148, 109–130.

Touboul, M., Kleine, T., Bourdon, B., Palme, H., Wieler, R., 2007. Late formation and prolonged differentiation of the Moon inferred from W isotopes in lunar metals. Nature 450, 1206–9.

Touboul, M., Kleine, T., Bourdon, B., Palme, H., Wieler, R., 2009. Tungsten isotopes in ferroan anorthosites: Implications for the age of the Moon and lifetime of its magma ocean. Icarus 199, 245–249.

Touboul, M., Liu, J., O'Neil, J., Puchtel, I.S., Walker, R.J., 2014. New insights into the Hadean mantle revealed by 182W and highly siderophile element abundances of supracrustal rocks from the Nuvvuagittuq Greenstone Belt, Quebec, Canada. Chemical Geology 383, 63–75.

Touboul, M., Puchtel, I.S., Walker, R.J., 2012. 182W evidence for long-term preservation of early mantle differentiation products. Science 335, 1065–9.

Trampert, J., Deschamps, F., Resovsky, J., Yuen, D., 2004. Probabilistic tomography maps chemical heterogeneities throughout the lower mantle. Science 306, 853–6.

Tucker, J.M., Mukhopadhyay, S., 2014. Evidence for multiple magma ocean outgassing and atmospheric loss episodes from mantle noble gases. Earth and Planetary Science Letters 393, 254–265.

Walter, M., Nakamura, E., Trø nnes, R., Frost, D., 2004. Experimental constraints on crystallization differentiation in a deep magma ocean. Geochimica et Cosmochimica Acta 68, 4267–4284.

Walter, M.J., Tronnes, R.G., 2004. Early Earth differentiation. Earth and Planetary Science Letters 225, 253–269.

Willbold, M., Elliott, T., Moorbath, S., 2011. The tungsten isotopic composition

of the Earth's mantle before the terminal bombardment. Nature 477, 195–8.
Williams, Q., Garnero, E.J., 1996. Seismic Evidence for Partial Melt at the Base of Earth's Mantle. Science 273, 1528–1530.

The following supplementary materials contain an example of the modified Monte Carlo algorithm (Table 1, Fig. 1), parameters used in radioactive decay equations (Table 2), example Sm, Nd, and Sm/Nd concentrations in the solid mantle pre and post overturn (Figs. 2 and 3), and partition coefficients used in the model (Figs. 4 and 5).

Example of the constrained Monte Carlo algorithm
Given the set of Sm-Nd partition coefficients for olivine in Table 1, the algorithm predicts 15,000 partition coefficients as shown in Supplementary Figure 1.

Supplementary Table 1 : Sm – Nd paired partition coefficients for olivine. PC = partition coefficient.

Reference	Sm PC	Nd PC	Sm/Nd PC
Frey, 1969	0.003	0.004	0.75
Shimizu et al., 1982	0.225	0.232	0.97
Shimizu et al., 1982	0.362	0.352	1.03
Shimizu et al., 1982	0.105	0.109	0.96
Shimizu et al., 1982	0.126	0.126	1.00
Mibe et al., 2006	0.00012	0.000029	4.14
Adam and Green, 2006	0.001	0.0005	2.00
Adam and Green, 2006	0.002	0.003	0.67
McKay, 1986	0.00058	0.00007	8.29
Fujimaki et al., 1984	0.0006	0.0003	2.00
Fujimaki et al., 1984	0.0108	0.0096	1.13
Fujimaki et al., 1984	0.0037	0.0023	1.61
Fujimaki et al., 1984	0.0088	0.0046	1.91
Fujimaki et al., 1984	0.0067	0.0069	0.97
Foley and Jenner, 2004	0.0016	0.00023	6.96
Kennedy et al., 1993	0.0011	0.00042	2.62
Kennedy et al., 1993	0.00062	0.0002	3.10
Kennedy et al., 1993	0.0023	0.0013	1.77
Kennedy et al., 1993	0.0082	0.0062	1.32
Larsen, 1979	0.318	0.355	0.90
Larsen, 1979	0.12	0.11	1.09
Larsen, 1979	0.087	0.085	1.02
McKenzie and O'Nions, 1991	0.0013	0.001	1.30
Nielsen et al., 1992	0.0011	0.0003	3.67
Paster et al., 1974	0.006	0.008	0.75
Schnetzler and Philpotts, 1970	0.011	0.01	1.10

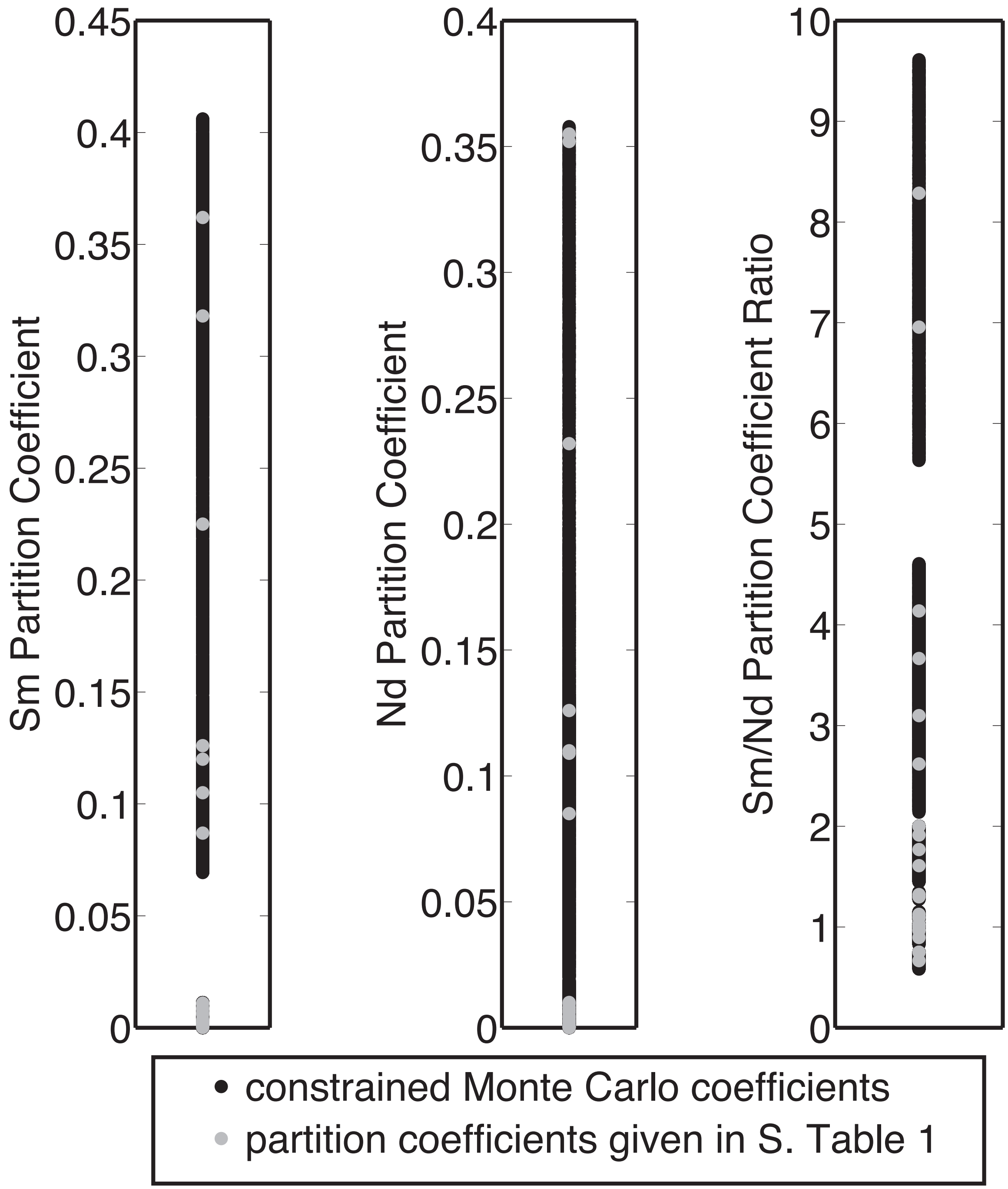

Supplementary Figure 1 : Constrained Monte Carlo partition coefficients given by the algorithm described in Section 2.2.2 for Sm and Nd in olivine. The randomly chosen coefficients cluster around the data given in Table 1.

Supplementary Table 2: Parameters use in radioactive decay calculations compiled from Carlson and Boyet, 2008, Kleine et al., 2009, Touboul et al., 2012, Kinoshita et al., 2012, and references therein.

$^{182}W/^{184}W$ standard	0.864863
$^{180}Hf/^{184}W$ CHUR	1.23
^{182}Hf $t_{1/2}$	8.9 Myr
$^{182}Hf/^{180}Hf$ CHUR	9.72e-5
$a^{180}Hf$	0.3508
$a^{184}W$	0.30642
$^{144}Sm/^{147}Sm$ CHUR	0.20503
$^{147}Sm/^{144}Nd$ CHUR	0.19600
$^{142}Nd/^{144}Nd$ CHUR	1.1418194
$^{142}Nd/^{144}Nd$ standard	1.14184
^{147}Sm $t_{1/2}$	106 Ga
$^{143}Nd/^{144}Nd$ CHUR standard	0.51263
$a^{147}Sm$	0.1499
$a^{144}Nd$	0.238
^{146}Sm $t_{1/2}$	68 Myr
$^{146}Sm/^{144}Sm$ CHUR	0.0094
OR	
^{146}Sm $t_{1/2}$	103 Myr
$^{146}Sm/^{144}Sm$ CHUR	0.008

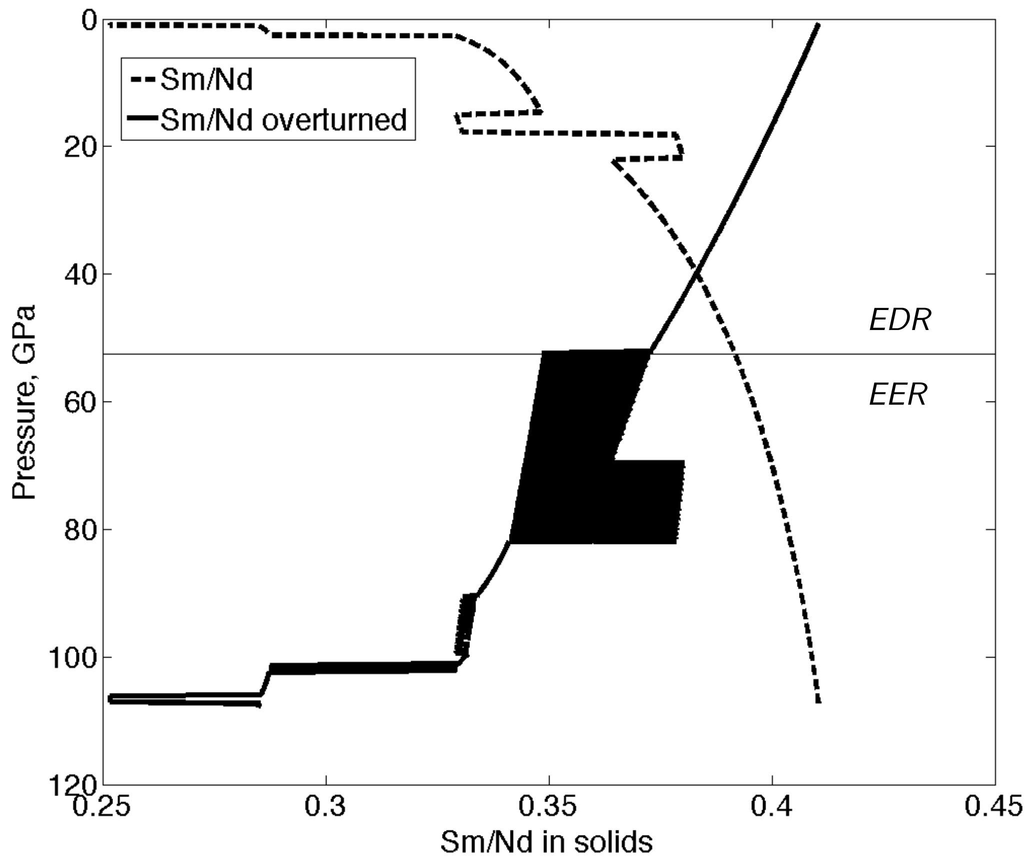

Supplementary Figure 2 : Sm/Nd ratio of solids pre and post overturn. The thin black horizontal line denotes R5, or the maximum EER thickness. This run, considered in the frame of the maximum EER, 5% interstitial liquid model varient using the shorter half-life of ^{146}Sm (68 Myr) is isotopically successful between 33 – 69 Myr. The ranges in μ^{142}Nd of the various reservoirs, depending on the timing of differentiation, are: EDR = 32 – 17 ppm, EER = -20 – 19 ppm, and the DAE = -3 – 5 ppm. The ε^{143}Nd of the DAE in this model is 11.

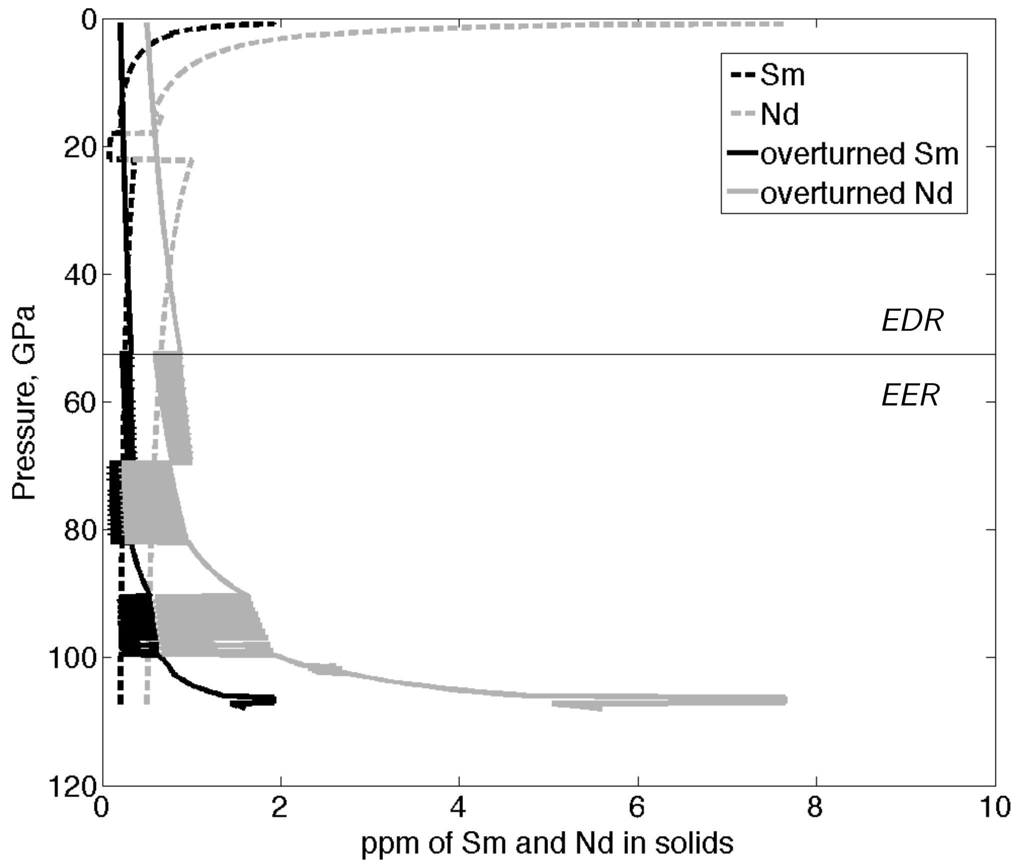

Supplementary Figure 3 : Sm and Nd ppm in solids pre and post overturn for the same model as in Supplementary Figure 2. The thin black horizontal line denotes R5, or the maximum EER thickness.

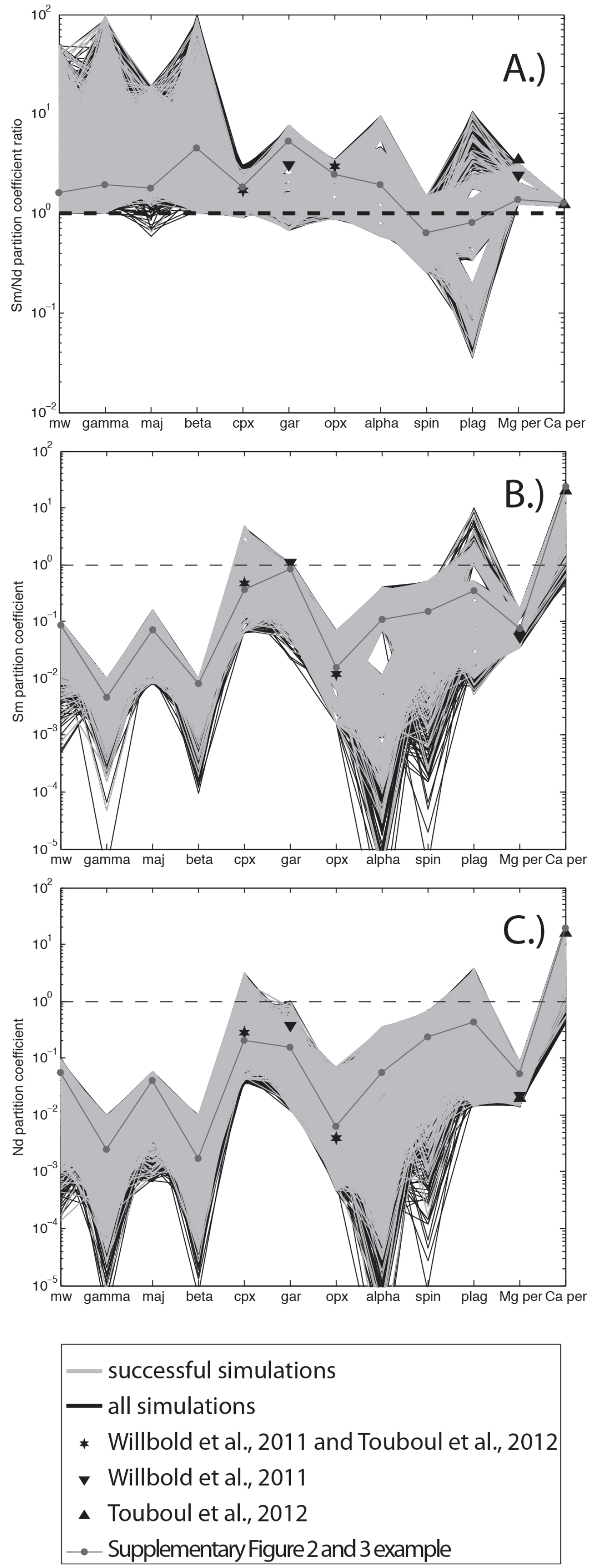

Supplementary Figure 4 : The Sm/Nd, Sm, and Nd partition coefficients and ratios of constrained-Monte Carlo simulations. The successful runs span the full range, which is why the black runs are not always visible. The mineral abbreviations are the same as Figure 2. The partition coefficients chosen resemble the clustering of partition coefficients in the database, not the outliers or the absolute range. For example, the highest Sm in plagioclase is 6.8, but only 29 simulations out of 15,000 reference that coefficient. The thin grey line represents the partition coefficients used in the example in Supplementary Figures 2 and 3.

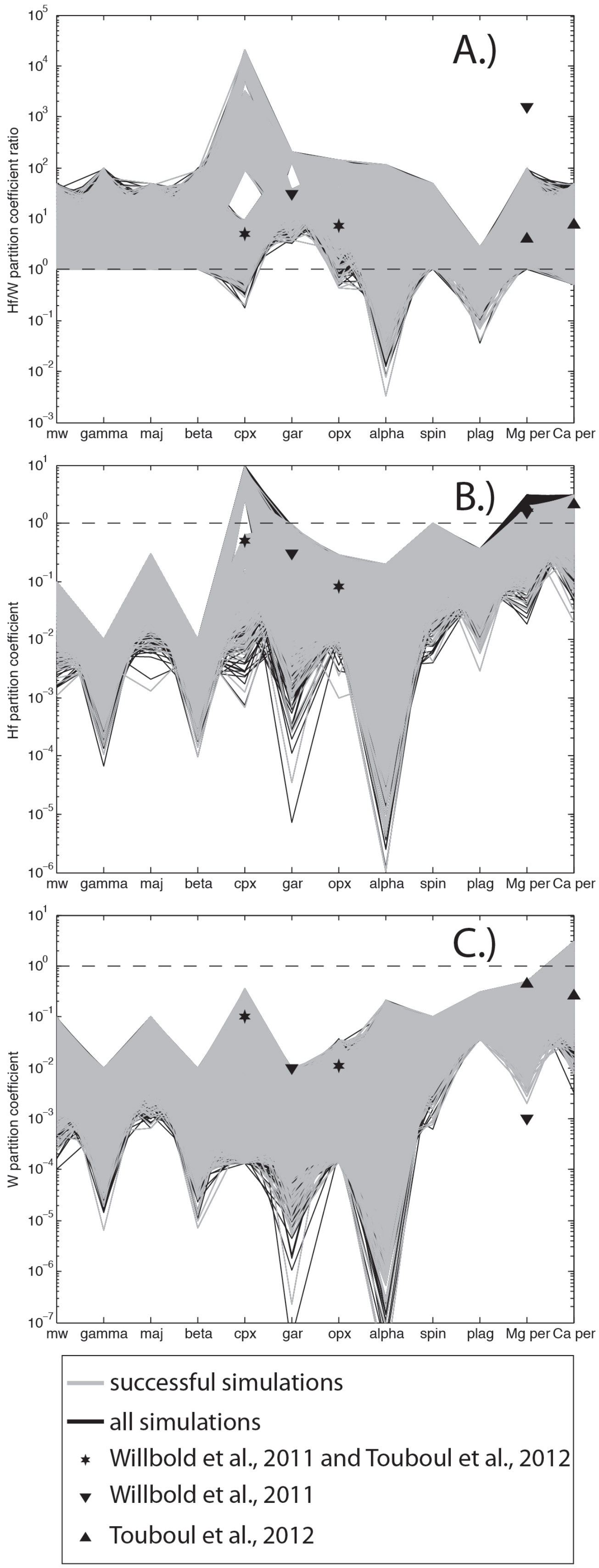

Supplementary Figure 5: The Hf/W, Hf, and W partition coefficients and ratios of constrained-Monte Carlo simulations. The successful runs span the full range, which is why the black runs are not always visible. The mineral abbreviations are the same as Figure 2. Notably, Hf cannot be too compatible (approx. > 2), or else the depleted reservoir will have more Hf than the enriched reservoir.

References

Adam, J., & Green, T. (2006). Trace element partitioning between mica- and amphibole-bearing garnet lherzolite and hydrous basanitic melt: 1. Experimental results and the investigation of controls on partitioning behaviour. Contributions to Mineralogy and Petrology 152, 1–17.

Carlson, R. W., & Boyet, M. (2008). Composition of the Earth's interior: the importance of early events. Phil. Trans. R. Soc. A 366, 4077–103.

Foley, S. F., & Jenner, G. A. (2004). Trace element partitioning in lamproitic magmas—the Gaussberg olivine leucitite. Lithos 75, 19–38.

Frey, F. (1969). Rare earth abundances in a high-temperature peridotite intrusion. Geochimica et Cosmochimica Acta 33, 1429–1447.

Fujimaki, H., Tatsumoto, M., & Aoki, K. (1984). Partition coefficients of Hf, Zr, and ree between phenocrysts and groundmasses. Journal of Geophysical Research 89(S02), B662-B672.

Kennedy, A. K., Lofgren, G. E., & Wasserburg, G. J. (1993). An experimental study of trace element partitioning between olivine, orthopyroxene and melt in chondrules: equilibrium values and kinetic effects. Earth and Planetary Science Letters 115, 177–195.

Kinoshita, N. Paul, M. Kashiv, Y. Collon, P. Deibel, C. M. DiGiovine, B. Greene, J. P. Henderson, D. J. Jiang, C. L. Marley, S. T. Nakanishi, T. Pardo, R. C. Rehm, K. E. Robertson, D. Scott, R. Schmitt, C. Tang, X. D. Vondrasek, R. Yokoyama, A. (2012). A Shorter 146Sm Half-Life Measured and Implications for 146Sm-142Nd Chronology in the Solar System. Science 335, 1614–1617.

Kleine, T., Touboul, M., Bourdon, B., Nimmo, F., Mezger, K., Palme, H., Jacobsen, S.B., Yin, Q., Halliday, A.N. (2009). Hf–W chronology of the accretion and early evolution of asteroids and terrestrial planets. Geochimica et Cosmochimica Acta 73, 5150–5188.

Larsen, L. M. (1979). Distribution of REE and other trace elements between phenocrysts and peralkaline undersaturated magmas, exemplified by rocks from the Gardar igneous province, south Greenland. Lithos 12, 303–315.

McKay, G. A. (1986). Crystal/liquid partitioning of REE in basaltic systems: Extreme fractionation of REE in olivine. Geochimica et Cosmochimica Acta 50, 69–79.

McKenzie, D., & O'Nions, R. K. (1991). Partial Melt Distributions from Inversion of Rare Earth Element Concentrations. Journal of Petrology 32(5), 1021–1091.

Mibe, K., Orihashi, Y., Nakai, S., & Fujii, T. (2006). Element partitioning between transition-zone minerals and ultramafic melt under hydrous conditions. Geophysical Research Letters 33, L16307.

Nielsen, R. L., Gallahan, W. E., & Newberger, F. (1992). Experimentally determined mineral-melt partition coefficients for Sc, Y and REE for olivine, orthopyroxene, pigeonite, magnetite and ilmenite. Contributions to Mineralogy and Petrology 110, 488–499.

Paster, T. P., Schauwecker, D. S., & Haskin, L. A. (1974). The behavior of some trace elements during solidification of the Skaergaard layered series. Geochimica et Cosmochimica Acta 38, 1549–1577.

Schnetzler, C., & Philpotts, J. A. (1970). Partition coefficients of rare-earth elements between igneous matrix material and rock-forming mineral phenocrysts—II. Geochimica et Cosmochimica Acta 34, 331–340.

Shimizu, H., Sangen, K., & Masuda, A. (1982). Experimental study on rare-earth element partitioning in olivine and clinopyroxene formed at 10 and 20kb for basaltic systems. Geochemical Journal 16, 107–117.

Touboul, M., Puchtel, I. S., & Walker, R. J. (2012). 182W evidence for long-term preservation of early mantle differentiation products. Science 335, 1065–9.